



Full length article

Mechanical characterization of human brain tissue



S. Budday^a, G. Sommer^b, C. Birkl^c, C. Langkammer^c, J. Haybaeck^d, J. Kohnert^a, M. Bauer^a, F. Paulsen^e, P. Steinmann^a, E. Kuhl^f, G.A. Holzapfel^{b,g,*}

^a Department of Mechanical Engineering, University of Erlangen-Nürnberg, 91058 Erlangen, Germany

^b Institute of Biomechanics, Graz University of Technology, 8010 Graz, Austria

^c Department of Neurology, Medical University of Graz, 8036 Graz, Austria

^d Department of Neuropathology, Institute of Pathology, Medical University of Graz, 8036 Graz, Austria

^e Chair of Anatomy II, University of Erlangen-Nürnberg, 91054 Erlangen, Germany

^f Departments of Mechanical Engineering & Bioengineering, Stanford University, CA 94305, USA

^g Norwegian University of Science and Technology (NTNU), Faculty of Engineering Science and Technology, 7491 Trondheim, Norway

ARTICLE INFO

Article history:

Received 26 July 2016

Received in revised form 24 October 2016

Accepted 25 October 2016

Available online 27 October 2016

Keywords:

Human brain
Mechanical testing
Hyperelastic modeling
Mooney Rivlin model
Ogden model

ABSTRACT

Mechanics are increasingly recognized to play an important role in modulating brain form and function. Computational simulations are a powerful tool to predict the mechanical behavior of the human brain in health and disease. The success of these simulations depends critically on the underlying constitutive model and on the reliable identification of its material parameters. Thus, there is an urgent need to thoroughly characterize the mechanical behavior of brain tissue and to identify mathematical models that capture the tissue response under arbitrary loading conditions. However, most constitutive models have only been calibrated for a single loading mode. Here, we perform a sequence of multiple loading modes on the same human brain specimen – simple shear in two orthogonal directions, compression, and tension – and characterize the loading-mode specific regional and directional behavior. We complement these three individual tests by combined multiaxial compression/tension-shear tests and discuss effects of conditioning and hysteresis. To explore to which extent the macrostructural response is a result of the underlying microstructural architecture, we supplement our biomechanical tests with diffusion tensor imaging and histology. We show that the heterogeneous microstructure leads to a regional but not directional dependence of the mechanical properties. Our experiments confirm that human brain tissue is nonlinear and viscoelastic, with a pronounced compression-tension asymmetry. Using our measurements, we compare the performance of five common constitutive models, neo-Hookean, Mooney-Rivlin, Demiray, Gent, and Ogden, and show that only the isotropic modified one-term Ogden model is capable of representing the hyperelastic behavior under combined shear, compression, and tension loadings: with a shear modulus of 0.4–1.4 kPa and a negative nonlinearity parameter it captures the compression-tension asymmetry and the increase in shear stress under superimposed compression but not tension. Our results demonstrate that material parameters identified for a single loading mode fail to predict the response under arbitrary loading conditions. Our systematic characterization of human brain tissue will lead to more accurate computational simulations, which will allow us to determine criteria for injury, to develop smart protection systems, and to predict brain development and disease progression.

Statement of Significance

There is a pressing need to characterize the mechanical behavior of human brain tissue under multiple loading conditions, and to identify constitutive models that are able to capture the tissue response under these conditions. We perform a sequence of experimental tests on the same brain specimen to characterize the regional and directional behavior, and we supplement our tests with DTI and histology to explore to which extent the macrostructural response is a result of the underlying microstructure. Results demonstrate that human brain tissue is nonlinear and viscoelastic, with a pronounced compression-tension asymmetry, and we show that the multiaxial data can best be captured by a modified version of the one-term Ogden model.

© 2016 Acta Materialia Inc. Published by Elsevier Ltd. All rights reserved.

* Corresponding author at: Institute of Biomechanics, Graz University of Technology, 8010 Graz, Austria.

E-mail address: holzapfel@tugraz.at (G.A. Holzapfel).

1. Introduction

Mechanical modeling is a promising tool to understand and predict the behavior of human brain tissue in health and disease [1]. The mechanics of the brain play not only an important role in injury such as traumatic brain injury [2] or shaken baby syndrome [3], but also in tumor growth [4] or during brain development [5–7]. Computational simulations enable us to determine criteria for injury [8], to develop smart protection systems such as helmets [9], or to predict brain development and disease progression [10,11]. However, such models require the development of constitutive laws calibrated with adequate experimental data to accurately relate tissue deformation to tissue stress.

Due to the ultrasoft and complex nature of brain tissue, biomechanical testing is challenging and former studies have reported controversial results. Shear moduli reported in the literature vary by an order of magnitude or more [12]. Recently, with enhanced sensitivity of the used testing devices, stiffness values now seem to converge in the range of 1 kPa [13]. Still, we are left with the controversy that different research groups find contrary results towards direction- [14–18], age- [13,19–22], and region-dependent properties [15,16,18,23–29] and towards the influence of post-mortem time [28,30–32]. Overall, the mechanical response of brain tissue is still far from being fully understood.

By reason of availability, only a few studies have actually tested human brain tissue [14,15,18,21,33–37]. Alternatively, researchers consulted porcine [13,15,16,38–42] or bovine brain tissue [26,28,30,43] due to their structural similarities with the human brain. Others tested the properties of rat [20,22,25] or mouse brains [44]. Most of those studies have focused on a specific type of loading. For example, human brain tissue has been tested *in vitro* under shear [14,18,21,33,36], compression [18,34,35,38], tension [18], and cyclic tension–compression [37] loadings, or *in vivo* using magnetic resonance elastography [23,24,27]. While these studies have significantly contributed to a better understanding of the material properties of the tissue, they remain insufficient to accurately describe its constitutive behavior under arbitrary loading conditions required for computational modeling. Systematic investigations of multiple loading modes remain sparse and have used different samples for each loading mode [18], which could influence the results, given the high regional, inter-specimen variation reported for brain tissue. In the present study, we sequentially test each specimen under multiple loading modes: shear in two orthogonal directions, compression, and tension.

The profound microstructural heterogeneity of brain tissue further raises the question to what extent constitutive models should account for regional and directional properties. It seems impractical to determine one set of material parameters valid for brain tissue as a whole. It is rather essential to understand how microstructural variations and anisotropy translate into the macroscopic mechanical response of the tissue and to systematically study regional and directional dependencies. Macroscopically, we can separate brain tissue into gray and white matter. Gray matter mostly consists of neurons responsible for data processing, and white matter of myelinated nerve fibers allowing a rapid signal transduction. However, our brain's microstructure varies significantly even within those two tissue types. For our study on the regional properties, we differentiate between tissue from the corpus callosum, the inner white matter mainly composed of highly aligned nerve fibers connecting both hemispheres; the corona radiata, the outer white matter composed of less aligned nerve fibers and glial cells; the basal ganglia, the deep gray matter; and the cortex. A similar distinction has previously been used to assess regional dependencies in porcine [15] and human [18] brain tissue. Regional variations in tissue stiffness can be of great interest for neurosurgeons or helmet designers as

more compliant regions are most likely more susceptible to injury. To find possible correlations between the macroscopic mechanical response and the underlying microstructure, we fix each specimen for histological staining upon completion of biomechanical testing. Furthermore, we compare histological images of tested and virgin specimens to ensure that the performed tests did not distort the tissue microstructure.

Another question that has not yet been satisfactorily answered is whether microstructural anisotropy due to the alignment of nerve fibers in white matter results in an anisotropic mechanical response, similar to the effect of collagen fibers in arterial tissue [45]. Previous studies on the directional properties have estimated fiber orientation from anatomical knowledge [15–18]. Here, for the first time, we combine biomechanical testing with diffusion tensor imaging and determine the orientation of nerve fibers prior to specimen extraction to guarantee a uniform fiber distribution throughout the tested sample. We test each sample under simple shear in two orthogonal directions, under unconfined compression and tension loadings to genuinely detect the contribution of nerve fibers for different loading modes. With the design of the current experimental study, we aimed to minimize the effects of nonuniform fiber distribution, nonuniform specimen dimensions, and inter-specimen variation, to unravel the controversy over both regional and directional properties.

Once we have understood the mechanical characteristics of brain tissue, the development of realistic finite element models is highly dependent on both the formulation of appropriate constitutive laws and the accurate identification of the corresponding material parameters. Generally, we face the problem of lacking experimental data suitable for detailed parameter estimation [46]. Constitutive parameters proposed in the literature have mostly been calibrated with experimental data from a single loading mode [40–42,47], but do not necessarily hold for arbitrary loading cases [38,48]. In the current study, we focus on the accurate characterization of the hyperelastic component of the mechanical response of brain tissue. We compare the applicability of five different constitutive models [49–52] to predict the behavior of brain tissue under multiple uniaxial loading modes and multiaxial loading cases. We simultaneously consider three loading modes, shear, compression, and tension, and test the validity of those constitutive models for combined compression/tension–shear loading [44,53].

Furthermore, we make use of calibrating constitutive models to make the experimental nonlinear stress–strain curves amenable to statistical analyses. Thus, we additionally calibrate the model that performed best, the one-term Ogden model, with each experimental curve separately to obtain one value for the shear modulus per specimen and loading mode. We emphasize that the purpose of those shear modulus calculations and their systematic comparison was to detect loading mode specific regional- and directional-dependencies such as the contribution of nerve fibers in compression versus tension, but not to determine material parameters appropriate for computational modeling of the brain.

The current experimental study provides not only novel insights into regional and directional dependencies but also yields essential information to construct realistic constitutive models capable of capturing the mechanics of the brain under multiaxial loading cases.

2. Materials and methods

2.1. Brain specimen

We obtained brain tissue from ten human cadavers during autopsy requested by the local health authorities with a post mortem interval of less than 24 h. The study was approved by the

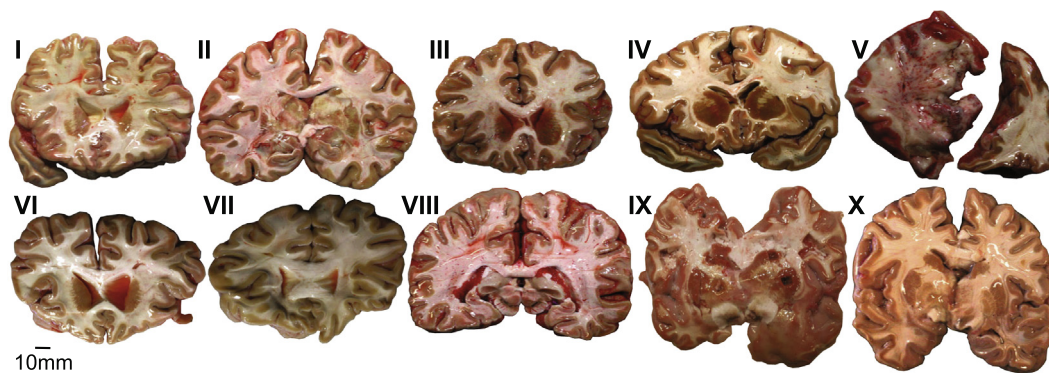


Fig. 1. Collection of the ten tested human brain slices. Brain V and VII did not include all structures of interest, as denoted in Table 1.

Table 1

Subject characteristics (brain number, age, gender, cause of death, and tested regions).

Brain no	Age (yrs)	Gender	Cause of death	Regions
I	69	Male	Metastasis	CC,CR,BG,C
II	54	Female	Myocardial infarction	CC,CR,BG,C
III	63	Male	Tumor progression	CC,CR,BG,C
IV	63	Male	Dilatation of the heart	CC,CR,BG,C
V	81	Female	Circulatory collapse	CR,C
VI	55	Female	Tumor progression	CC,CR,BG,C
VII	63	Male	Myocardial infarction	CC,CR,C
VIII	68	Male	Dilatation of the heart	CC,CR,BG,C
IX	78	Male	Cardiorespiratory insufficiency	CC,CR,BG,C
X	68	Male	Cardiorespiratory insufficiency	CC,CR,BG,C

CC = corpus callosum; CR = corona radiata; BG = basal ganglia; C = cortex.

Ethics Commission of the Medical University of Graz, Austria, with the approval number 25–420 ex 12/13. Immediately after autopsy, we first performed magnetic resonance imaging (MRI) including diffusion tensor imaging (DTI) of each brain to assess the fiber orientation. After MRI, we cut the brain into approximately 1 cm thick coronal slices. We prepared one slice of each brain, including the corpus callosum and the basal ganglia, if possible, see Fig. 1, to perform biomechanical testing. In Table 1, we summarize the subject characteristics of all tested brains. The subject age ranged from 54 to 81 years with an average age of 66 years at the time of death. Although the current study was not designed to investigate the effects of gender, age, or disease, we will briefly discuss potential influences of those factors in Section 4. None of the subjects had suffered from any neurological disease known to affect the microstructure of the brain, such as Alzheimer's disease.

We kept the tissue refrigerated at 3 °C and humidified with phosphate-buffered saline solution at all times to minimize tissue degradation. We tested all samples within 48 h after subject acquisition. This results in a total post mortem interval between death and the end of biomechanical testing of less than 60 h.

2.2. Magnetic resonance imaging

MR images were acquired with a 3 Tesla whole body system (Magnetom PRISMA, Siemens Healthcare, Erlangen, Germany) using a head coil array with 32 elements. Structural MR imaging included a

T2 weighted sequence (repetition time TR = 4870 ms, echo times TE = 11 and 77 ms, in plane resolution = 1 × 1 mm², 2 mm slice thickness and FOV = 256 mm) and a T1 weighted 3D MPRAGE sequence with 1 mm isotropic resolution (TR = 1900 ms, TE = 2.79 ms, TI = 350 ms and FOV = 230 mm). Diffusion weighted images (DWI) were acquired using a readout segmented echo planar imaging (EPI) sequence (TR = 3100 ms, TE = 55 ms, FOV = 180 mm, resolution = 1 × 1 × 5 mm³, 25 slices, b = 1500 s/mm², 12 diffusion directions, 11 readout segments, EPI echo spacing = 0.34 ms, 2 averages and GRAPPA acceleration factor R = 3). The total acquisition time for all sequences was approximately 25 min.

2.2.1. Diffusion tensor imaging

Diffusion MRI can depict the Brownian motion of hydrogen protons in tissue. However, microstructural barriers in human tissue such as from white matter fiber bundles hamper unrestricted diffusion, and consequently result in an anisotropic diffusion pattern, which can be assessed by DTI. By applying diffusion sensitizing gradient in at least six independent spatial directions, a full second rank diffusion tensor can be calculated. Geometrical distortions induced by eddy currents were corrected by affine co-registration of the diffusion weighted images using the FMRIB Software Library (FSL v4.2) [54,55] and the DWI measurements from 12 directions were used to pixelwise calculate the DTI tensor model by using FSL. The diffusion tensor can be described by an ellipsoid with three axes. Those axes are represented by the eigenvectors and

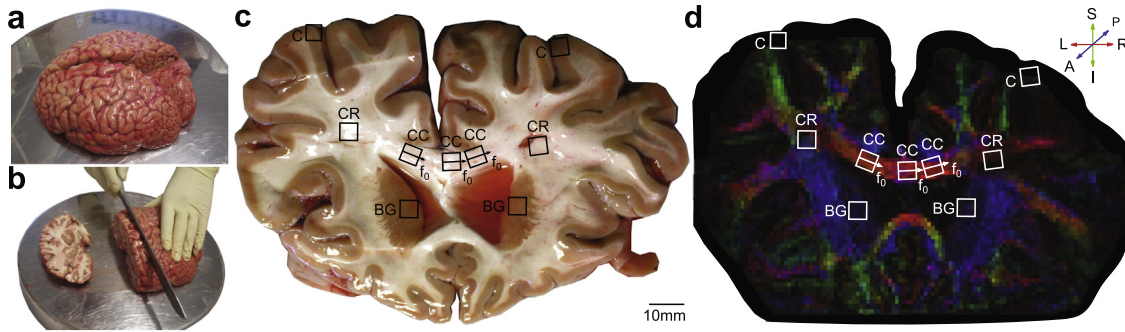


Fig. 2. Preparation of specimens for biomechanical testing: (a) typical human brain obtained after autopsy; (b) cutting the brain in coronal slices; (c) locations of specimen extraction from four brain regions, the corpus callosum (CC), the corona radiata (CR), the basal ganglia (BG) and the cortex (C), exemplary shown for brain VI. The arrows indicate the nerve fiber direction f_0 for the specimens from the CC; (d) RGB color-coded FA image of the tested tissue slice. Green color indicates nerve fiber bundles running in the superior (S) – inferior (I) direction, red color indicates fiber bundles running in the left (L) – right (R) direction, and blue color indicates an anterior (A) – posterior (P) direction.

their lengths are given by the according eigenvalues; λ_1 denotes the biggest, λ_2 and λ_3 the smaller eigenvalues. The eigenvector associated with λ_1 represents the principal direction of the diffusion ellipsoid, which is physically corresponding to the direction of the white matter fiber bundle.

The most significant parameter of DTI is the fractional anisotropy FA defined as

$$FA = \frac{\sqrt{3[(\lambda_1 - \langle \lambda \rangle)^2 + (\lambda_2 - \langle \lambda \rangle)^2 + (\lambda_3 - \langle \lambda \rangle)^2]}}{\sqrt{2(\lambda_1^2 + \lambda_2^2 + \lambda_3^2)}} \quad (1)$$

In brief, FA, also entitled as neuronal integrity, is normalized between 0 and 1, where 0 describes entirely isotropic diffusion and 1 entirely anisotropic diffusion. Fig. 2d shows an RGB color-coded FA image, with FA represented as brightness and the colors represent the orientation of neuronal fiber bundles. Generally, FA is higher in fiber bundles with a high density of axons and commonly FA values >0.2 are considered as directed fiber bundles. In this study we included highly anisotropic anatomical regions with high FA such as the corpus callosum (CC) and the corona radiata (CR), and additionally we included the cortex (C) and the basal ganglia (BG), which have lower FA, and therefore almost isotropic diffusion properties when assessed by diffusion MRI. However, until now it remained unclear whether diffusion anisotropy assessed by MRI is linked to the biomechanical properties of the human brain tissue.

2.3. Specimen preparation

As the current experiments were inter alia designed to unravel the ongoing controversy regarding regional and directional properties of brain tissue, we carefully chose the location, orientation, and size of samples. We differentiate between four regions, the corpus callosum (CC), white matter with high fiber density, mostly consisting of uniaxially oriented nerve fiber bundles running between the two hemispheres, the corona radiata (CR), (the outer) white matter with lower fiber density, the basal ganglia (BG), and the cortex (C). Fig. 2c shows the location of all specimens extracted from brain VI.

We chose specimen dimensions of $5 \times 5 \times 5$ mm, restricted by the maximum cortical thickness of 5 mm. We excised the tissue specimens with a scalpel and kept all tools and gloves humidified with phosphate-buffered saline solution to ensure the tissue did not adhere and tear during handling. Due to the particularly soft

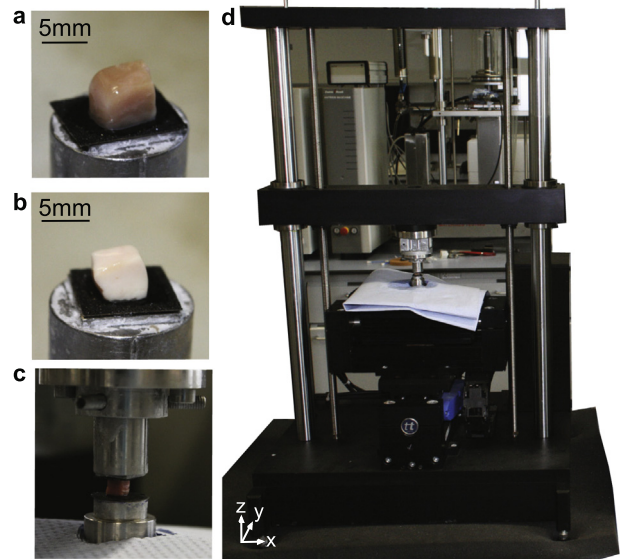


Fig. 3. (a) Representative gray matter brain tissue cube of ~5 mm side length glued to the upper specimen holder; (b) representative white matter brain tissue cube of ~5 mm side length; (c) sample glued to the upper and lower specimen holder of the triaxial testing device; (d) specimen inserted in the setup, hydrated with phosphate-buffered saline solution, and ready for testing.

nature of brain tissue, the samples deformed under their own weight during preparation and mounting, which led to a variation in final sample dimensions with an edge length ranging from 3 to 7 mm and a specimen height ranging from 2 to 5 mm. We extracted two specimens from the corona radiata, the basal ganglia, and the cortex (one from each hemisphere), and three specimens from the corpus callosum to increase the number of data points for the study on directional properties. In some cases, we were unable to extract the desired number of specimens, since the obtained slice did not include all regions of interest (indicated in Fig. 1 and the right column of Table 1), it was not possible to extract more than one reasonably sized specimens from a certain region, or that specimens broke during handling or testing.

We excised and prepared each sample shortly before testing to limit degradation and alterations in the tissue. Throughout the preparation process, we humidified the specimens with phosphate-buffered saline solution to avoid dehydration. We fixed

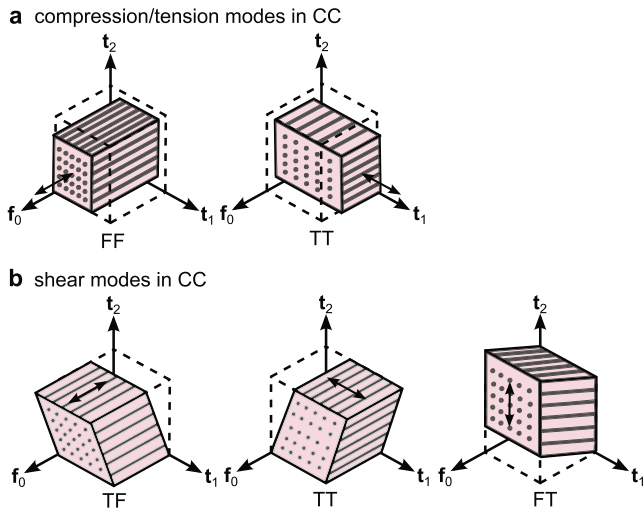


Fig. 4. (a) Two possible compression and tension modes, along (FF) and transverse (TT) to the nerve fiber direction \mathbf{f}_0 for specimens taken from the corpus callosum (CC); (b) three simple shear modes ij , for $i, j \in \{T, F\}$, where i denotes the normal vector of the face that is shifted by simple shear and j denotes the direction of shear, along (F) or transverse (T) to the fiber direction \mathbf{f}_0 .

a comparable tissue cube adjacent to the tested specimens in 4% Formaldehyde solution for histological investigation. This allowed us to detect any changes in the tissue's microstructure due to biomechanical testing or due to the usage of cyanoacrylate adhesive to attach the samples to the testing device.

2.4. Experimental setup

After extraction and preparation, we glued each sample to the upper specimen holder with a thin layer of cyanoacrylate adhesive, as illustrated in Fig. 3a and b. To increase the glued surface, we used a piece of sand paper with an average particle diameter of $58.5 \mu\text{m}$. We measured the dimension of each sample prior to testing to determine the reference configuration to calculate the stretch, the amount of shear, and stresses during loading. We inserted the specimen in the triaxial testing device, provided a thin layer of adhesive to the lower specimen holder, and lowered the upper specimen holder with the sample until we detected a preload of about 10 mN. After a hardening period of 300 s, we slowly reduced the preload to 0 mN and adjusted the relative position of the plates in the x - and y -directions to obtain zero forces. This state

illustrated in Fig. 3c was considered the unloaded configuration. Before we started the actual test, we carefully humidified the sample with phosphate-buffered saline solution; the surface tension of water kept the phosphate-buffered saline solution between the upper and lower specimen holder, as shown in Fig. 3d, and maintained the specimens hydrated throughout the entire test procedure. After hydration, all forces were set to zero again to compensate for the force which the liquid exerted on the upper specimen holder. We conducted all tests at room temperature. Testing in a bath of tempered solution at body temperature would have precluded unmounting of the tested sample for microstructural investigation and would have increased the risk that samples soaked and changed properties during the course of the test.

As specimens from the corpus callosum exhibited a uniform nerve fiber orientation \mathbf{f}_0 , we distinguished between three different modes in simple shear and two different modes in compression and tension, as illustrated in Fig. 4. In the case of compression and tension, the upper platform moves in the z -direction. In the case of shear, the lower platform moves relative to the fixed upper platform using a biaxial translation stage in the x - and y -directions, as denoted in Fig. 3d. The system operates with a stroke resolution of $0.04 \mu\text{m}$ in the z -direction and with a stroke resolution of $0.25 \mu\text{m}$ in the x - and y -directions [56]. We recorded the resulting forces in three orthogonal directions (x, y, z) simultaneously with a 3-axes force-sensor (K3D40, ME-Measuring Equipment, Henningsdorf, Germany). We achieved motor control and data acquisition using the software testXpert II Version 3.2 (Zwick/Roell GmbH & Co. KG, Ulm, Germany) on a Windows-based personal computer.

We conducted two different testing protocols, as summarized in Tables 2 and 3: in the first protocol, we performed a sequence of different loading modes, shear, compression, and tension, to assess regional and directional dependencies and to determine the corresponding constitutive parameters for computational modeling; in the second protocol, we performed simple shear experiments superimposed by compressive and tensile loadings to validate the constitutive parameters for multiaxial loading cases.

We chose quasi-static loading conditions with a speed of $v = 2 \text{ mm/min}$. We applied three cycles per loading mode, where two cycles served for pre-conditioning and the third cycle was used for further data analysis. This allowed us to obtain a repeatable and comparable response for all loading modes conducted consecutively on one sample. Preliminary investigations had shown that two pre-conditioning cycles were the optimal number to guarantee a repeatable mechanical response while minimizing the risk of damage in the highly fragile tissue. As we consecutively

Table 2

Testing protocol for sequential testing.

Protocol 1: Sequence of multiple loading modes
<ul style="list-style-type: none"> • Simple shear in x-direction up to an amount of shear of $\gamma = 0.2$: 2 pre-conditioning + 1 main cycle • Stress relaxation in x-direction at $\gamma = 0.2$: 300 s holding • Simple shear in y-direction up to an amount of shear of $\gamma = 0.2$: 2 pre-conditioning + 1 main cycle • Relaxation in y-direction at $\gamma = 0.2$: 300 s holding • Unconfined compression up to 10% strain: 2 pre-conditioning + 1 main cycle • Stress relaxation at 10% compressive strain: 300 s holding • Uniaxial tension up to 10% strain: 2 pre-conditioning + 1 main cycle

Table 3

Testing protocol for combined testing.

Protocol 2: Combined compression/tension-shear loading
<ul style="list-style-type: none"> • Simple shear up to an amount of shear of $\gamma = 0.2$ in two orthogonal directions (2 pre-conditioning + 1 main) superimposed on increasing compressive strain from 0 to 25% in 5% increments • Simple shear up to an amount of shear of $\gamma = 0.2$ in two orthogonal directions (2 pre-conditioning + 1 main) superimposed on increasing tensile strain from 5 to 25% in 5% increments

tested each specimen under multiple loading modes, we further had to pay particular attention not to damage the tissue and alter its mechanical response during the course of the test. Thus, we significantly reduced the maximum strain applied compared to previous studies [18].

In detail, the first protocol consisted of a sequence of different loading modes starting with sinusoidal simple shear up to an amount of shear of $\gamma = 0.2$ in two orthogonal directions, where the amount of shear γ specifies the relative in-plane displacement of two parallel layers in the material body divided by their separation distance. Thus, the maximum displacement of the lower stage in x - and y -directions yields $\Delta x = \Delta y = 0.2H$ with specimen height H . Upon completion of each direction, we conducted relaxation tests to probe the viscoelastic properties of the tissue. Therefore, we applied a rapid shear step up to $\gamma = 0.2$ with a speed of $v = 100$ mm/min and recorded the resulting forces for a period of 300 s. The shear tests were followed by an unconfined uniaxial compression test up to 10% compressive strain, a relaxation test of 300 s holding at 10% compression, and a uniaxial extension test up to 10% tensile strain. We obtained results from protocol 1 for a total of $n = 71$ samples, where 20 samples were excised from the corpus callosum, 18 from the corona radiata, 15 from the basal ganglia, and 18 from the cortex.

The second protocol consisted of combined compression/tension-shear loading. We first increased the compressive strain from 0 to 25% in increments of 5%, and subsequently the tensile strain from 5 to 25%, again in increments of 5%; at each axial stretch level, we applied a sinusoidal simple shear up to $\gamma = 0.2$ in two orthogonal directions. Similar to protocol 1, we conducted three cycles per stretch level and direction. Due to the long time duration of the combined loading protocol, it was challenging to keep specimens hydrated at all times. When the specimens dried out as hydration had evaporated or drained, tissue properties changed notably and we decided not to include the results in our analysis. We performed protocol 2 only for 4 samples from the corona radiata.

2.5. Histological staining

Following biomechanical testing, we fixed each specimen using 4% Formaldehyde solution. We replaced tissue water with alcohol, cleared the samples by replacing alcohol with xylene, and embedded the dehydrated samples in paraffin wax blocks. For one representative specimen from each region of brain VI, we prepared 8–10 μm thick histological slices. We used two different stains to reveal the underlying microstructure, Klüver-Barrera and Gomori silver. The Klüver-Barrera stain colors myelin wrapped around nerve fibers in blue, neuropil in pink, and nerve cells in purple. The Gomori silver stain colors cell nuclei and interconnections including axons and dendrites, which are too slender and transparent to be seen in the Klüver-Barrera stain, in black. All imaging was performed on a confocal microscope.

2.6. Data analysis and constitutive modeling

To describe the macroscopic deformation of each tested tissue cube, we used the nonlinear equations of continuum mechanics and introduced the deformation map $\varphi(\mathbf{X})$ which maps tissue from the undeformed, unloaded configuration to the deformed, loaded configuration [52]. The deformation gradient $\mathbf{F}(\mathbf{X}) = \nabla_{\mathbf{X}}\varphi(\mathbf{X})$ maps undeformed line elements to deformed line elements, where \mathbf{X} and \mathbf{x} denote the position vectors in the unloaded and loaded configurations, respectively. The principal stretches $\lambda_i, i = 1, 2, 3$ (not to be confused with the eigenvalues introduced in Section 2.2.1), are the square roots of the eigenvalues of the left and right Cauchy–Green tensors defined by $\mathbf{b} = \mathbf{F}\mathbf{F}^T$ and $\mathbf{C} = \mathbf{F}^T\mathbf{F}$, where $[\mathbf{F}] = \text{diag}\{\lambda_1, \lambda_2, \lambda_3\}$.

We assumed that the tissue cubes deformed homogeneously and that brain tissue was incompressible characterized by $\det \mathbf{F} = 1$.

2.6.1. Simple shear

To quantify the shear response of each specimen, we computed the amount of shear γ and the corresponding shear stress. We assumed that the cross-section of the specimen remained unchanged during simple shear and determined the shear stresses $\tau_{xz/yz} = P_{xz/yz} = f/A$ as the shear force f , the force recorded in the direction of shear, divided by the shear area $A = WL$ with the specimen length L and specimen width W . The deformation gradient \mathbf{F} for simple shear in the first direction takes on the matrix form

$$[\mathbf{F}] = \begin{bmatrix} 1 & 0 & \gamma \\ 0 & 1 & 0 \\ 0 & 0 & 1 \end{bmatrix}, \quad (2)$$

with the principal stretches

$$\lambda_{1/2} = \frac{\gamma}{2} \pm \sqrt{1 + \frac{\gamma^2}{4}} \quad \text{and} \quad \lambda_3 = 1. \quad (3)$$

2.6.2. Uniaxial compression/tension

In uniaxial compression and tension we computed the stretch $\lambda = 1 + \Delta z/H$ with specimen height H and z -displacement Δz . The first Piola–Kirchhoff stress P_{zz} is the force f_z divided by the cross-sectional area A of the specimen in the unloaded reference configuration, i.e. $P_{zz} = f_z/A$. We assumed that the tissue cubes deformed uniformly under unconfined compression and extension, so that the deformation gradient \mathbf{F} takes on the matrix form

$$[\mathbf{F}] = \begin{bmatrix} 1/\sqrt{\lambda} & 0 & 0 \\ 0 & 1/\sqrt{\lambda} & 0 \\ 0 & 0 & \lambda \end{bmatrix}, \quad (4)$$

with the principal stretches

$$\lambda_1 = \lambda_2 = \frac{1}{\sqrt{\lambda}} \quad \text{and} \quad \lambda_3 = \lambda. \quad (5)$$

2.6.3. Combined loading

For combined compression/tension-shear tests, we superimposed simple shear with the amount of shear γ on the axial stretch λ . For a constant amount of shear, the maximum shear displacements in the x - and y -directions decrease with increasing compressive strain and increase with increasing tensile strain as $\Delta x = \Delta y = \gamma/\lambda H$. We calculated the shear stresses by dividing the force recorded in the direction of shear by the initial shear area $\tau_{xz/yz} = P_{xz/yz} = f/A$. In the combined loading case, the deformation gradient \mathbf{F} becomes the matrix form

$$[\mathbf{F}] = \begin{bmatrix} 1/\sqrt{\lambda} & 0 & \lambda\gamma \\ 0 & 1/\sqrt{\lambda} & 0 \\ 0 & 0 & \lambda \end{bmatrix}, \quad (6)$$

with the principal stretches

$$\lambda_1 = \frac{1}{\sqrt{\lambda}} \quad \text{and} \quad \lambda_{2,3} = \sqrt{\frac{\lambda^3 + \lambda^3\gamma^2 + 1 \pm \theta}{2\lambda}}, \quad (7)$$

$$\text{with } \theta = \sqrt{\lambda^6 + 2\lambda^6\gamma^2 - 2\lambda^3 + \lambda^6\gamma^4 + 2\lambda^3\gamma^2 + 1}.$$

2.6.4. Constitutive modeling

Based on our experimental findings presented in the Results, Section 3.2, we assumed an isotropic material response. We further focused on the time-independent, hyperelastic response of brain

tissue and neglected its time-dependent, viscous or porous contributions. We adopted several widely used phenomenological hyperelastic strain-energy functions to relate the stretch or amount of shear to the corresponding stress.

We considered three special cases of the generalized Ogden model with the strain-energy function $\Psi = \sum_{i=1}^n \mu_i (\lambda_1^{\alpha_i} + \lambda_2^{\alpha_i} + \lambda_3^{\alpha_i} - 3) / \alpha_i$ [49], where the constitutive parameters α_i correspond to the strain-magnitude sensitive nonlinear characteristics of the tissue. The classical shear modulus, known from the linear theory, is given by $\mu = 1/2 \sum_{i=1}^n \mu_i \alpha_i$ [52]. We adopted the neo-Hookean constitutive model with $\alpha_1 = 2$ and $\mu_1 = \mu$, the Mooney–Rivlin constitutive model with $\alpha_1 = 2, \mu_1 = C_1 = \mu - C_2, \alpha_2 = -2$ and $\mu_2 = C_2$, and the one-term Ogden model, where we reformulated the strain-energy function in terms of the classical shear modulus $\mu = \alpha_1 \mu_1 / 2$ and the parameter $\alpha = \alpha_1$. In addition, we considered an exponential strain-energy function proposed by Demiray [50] and a rapidly strain-stiffening constitutive model proposed by Gent [51]. The strain-energy functions of all considered hyperelastic models expressed in terms of the principal stretches take on the forms

$$\Psi^{\text{N-H}} = \frac{1}{2} \mu (\lambda_1^2 + \lambda_2^2 + \lambda_3^2 - 3), \quad (8)$$

$$\Psi^{\text{M-R}} = \left(\frac{1}{2} \mu - C_2 \right) (\lambda_1^2 + \lambda_2^2 + \lambda_3^2 - 3) + C_2 (\lambda_1^{-2} + \lambda_2^{-2} + \lambda_3^{-2} - 3), \quad (9)$$

$$\Psi^{\text{Dmr}} = \frac{1}{2} \mu \{ \exp[\beta (\lambda_1^2 + \lambda_2^2 + \lambda_3^2 - 3)] - 1 \} / \beta, \quad (10)$$

$$\Psi^{\text{Gnt}} = -\frac{1}{2} \mu \eta \ln[1 - (\lambda_1^2 + \lambda_2^2 + \lambda_3^2 - 3) / \eta], \quad (11)$$

$$\Psi^{\text{Ogd}} = 2\mu (\lambda_1^\alpha + \lambda_2^\alpha + \lambda_3^\alpha - 3) / \alpha^2. \quad (12)$$

We can express the first Piola–Kirchhoff stress tensor \mathbf{P}^Ψ as the derivative of the strain-energy function Ψ with respect to the deformation gradient \mathbf{F} [52]. For an incompressible hyperelastic material with $\det \mathbf{F} = 1$, we obtain

$$\mathbf{P}^\Psi = \frac{\partial \Psi}{\partial \mathbf{F}} - p \mathbf{F}^{-\text{T}} = \sum_{i=1}^3 \frac{\partial \Psi}{\partial \lambda_i} \mathbf{n}_i \otimes \mathbf{N}_i - p \mathbf{F}^{-\text{T}}, \quad (13)$$

where \mathbf{n}_i and \mathbf{N}_i are the eigenvectors of the left and right Cauchy–Green tensors, respectively, and p serves as a Lagrange multiplier. While the shear stresses in simple shear and combined loading are independent of p , in unconfined compression and tension, we determined p by evaluating the condition $P_{xx} = P_{yy} = 0$. The derivatives of the strain-energy functions Eqs. (8)–(12) with respect to the principal stretches yield

$$\frac{\partial \Psi^{\text{N-H}}}{\partial \lambda_i} = \mu \lambda_i, \quad (14)$$

$$\frac{\partial \Psi^{\text{M-R}}}{\partial \lambda_i} = (\mu - 2C_2) \lambda_i - 2C_2 / \lambda_i^3, \quad (15)$$

$$\frac{\partial \Psi^{\text{Dmr}}}{\partial \lambda_i} = \mu \exp[\beta (\lambda_1^2 + \lambda_2^2 + \lambda_3^2 - 3)] \lambda_i, \quad (16)$$

$$\frac{\partial \Psi^{\text{Gnt}}}{\partial \lambda_i} = \mu \eta (\eta - \lambda_1^2 - \lambda_2^2 - \lambda_3^2 + 3)^{-1} \lambda_i, \quad (17)$$

$$\frac{\partial \Psi^{\text{Ogd}}}{\partial \lambda_i} = 2\mu \lambda_i^{\alpha-1} / \alpha, \quad (18)$$

for $i = 1, 2, 3$.

To calibrate the constitutive parameters, we used the nonlinear least-squares algorithm *lsqnonlin* in MATLAB. In a first step, we calibrated the constitutive models with the average experimental data over different regions or directions from each loading mode – shear, compression, and tension – separately to obtain one set of material parameters per loading mode. We minimized the objective function

$$\chi^2 = \sum_{i=1}^n (P_{az} - P_{az}^y)^2, \quad (19)$$

where n is the number of considered experimental data points, denoted by black dots in Fig. 15, while P_{az} and P_{az}^y with the directions $a = x, y, z$ are the experimentally determined and model predicted first Piola–Kirchhoff stresses, respectively. In addition, we used each individual experimental curve separately for calibration of the modified one-term Ogden model to make the nonlinear stress–strain curves amenable to statistical analyses by comparing the shear moduli μ .

In a second step, we calibrated the constitutive models with the average experimental data of all loading modes simultaneously to obtain one set of material parameters that not only holds for a single loading mode but for all loading conditions performed in protocol 1. In this case, we minimized the objective function

$$\chi^2 = \sum_{i=1}^{n_s} (P_{xz} - P_{xz}^y)^2 + \sum_{i=1}^{n_c+n_t} (P_{zz} - P_{zz}^y)^2, \quad (20)$$

where n_s, n_c , and n_t denote the number of considered experimental data points for shear, compression, and tension loading, respectively.

In a last step, we calibrated the model that performed best in the previous step, the one-term Ogden model, with data from combined compression/tension-shear loadings in protocol 2 to investigate whether this constitutive model is also able to capture the tissue response under combined loading conditions. Considering the average shear stress versus amount of shear curves of all 11 axial stretch levels (see Table 3) simultaneously, we minimized the objective function

$$\chi^2 = \sum_{k=1}^{11} \sum_{i=1}^n (P_{xz,k} - P_{xz}^y(\lambda_k))_i^2, \quad (21)$$

where

$$\lambda_k = 1.00, 0.95, 0.90, 0.85, 0.80, 0.75, 1.05, 1.10, 1.15, 1.20, 1.25.$$

To evaluate the ‘goodness of fit’, we determined the coefficient of determination $R^2 = 1 - S^{\text{res}} / S^{\text{tot}}$, where $S^{\text{res}} = \sum_{i=1}^n (P_i - P_i^y)^2$ is the sum of squares of residuals with the experimental data values P_i , the corresponding model data values P_i^y , and the number of data points n , and $S^{\text{tot}} = \sum_{i=1}^n (P_i - \bar{P})^2$ is the total sum of squares with the mean of the experimental data $\bar{P} = 1/n \sum_{i=1}^n P_i$.

2.7. Statistical analysis

To reveal significant regional and directional dependencies in the mechanical properties of brain tissue, we statistically evaluated the experimental data. To assess elastic tissue properties, we compared shear moduli obtained from calibrating the modified one-term Ogden model with each experimental stress–strain curve separately as described in Section 2.6.4; to assess viscoelastic properties, we compared stress relaxation percentages after 5 min as well as hysteresis areas during cyclic loading. We performed all statistical analyses with the Statistics Toolbox in MATLAB and considered a p -value lower than 0.05 to be significant. We executed pairwise t -tests for all possible comparisons of means in different directions (TF, TT, and FT in shear; FF and TT in compression and

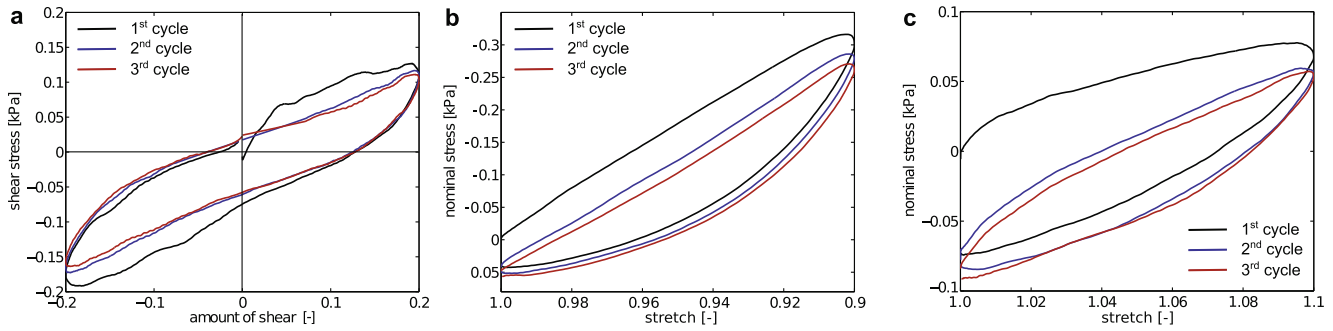


Fig. 5. Representative pre-conditioning behavior in shear (a), compression (b), and tension (c) for a specimen from the corona radiata of brain VIII; the tissue exhibits a large hysteretic response with substantial pre-conditioning during the first loading cycle, which is more pronounced in compression and tension than in shear. The subsequent cycles display only minor differences, wherein the ‘elastic’ response (averaged curve between loading and unloading) remains constant.

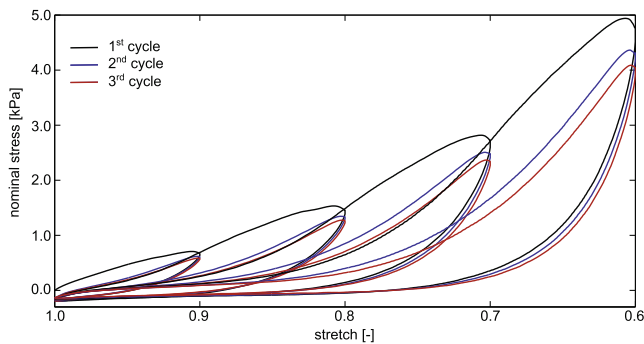


Fig. 6. Representative nominal stress versus stretch behavior of one specimen from the corona radiata of brain VIII for increasing compressive strain from 0.1 to 0.4 in steps of 0.1 – three cycles per stretch level. The tissue exhibits substantial pre-conditioning during the first cycle of each stretch level, and successively softens with increasing compression.

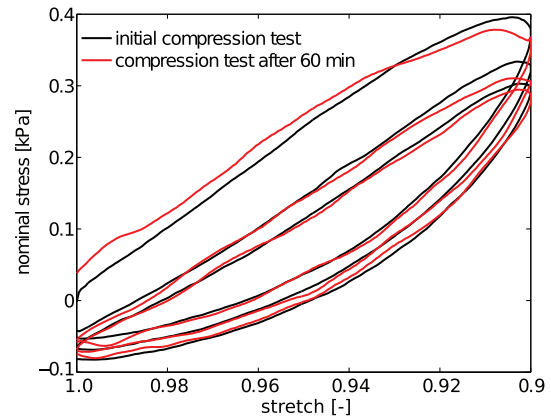


Fig. 7. Representative nominal stress versus stretch behavior of a specimen from the corona radiata of brain IX loaded twice with a set of three cycles up to 10% compressive strain separated by a 60 min recovery period. The tissue exhibited a similar pre-conditioning pattern for both compression tests.

tension, as denoted in Fig. 4) and different regions (corpus callosum, corona radiata, basal ganglia, and cortex) in shear, compression, and tension. As this procedure postulates specifying a significance level of 0.05 for each comparison without accounting for the fact that we increase the chance of incorrectly finding a significant difference with the number of comparisons, we additionally performed separate Tukey–Kramer tests for multiple comparisons – one per loading mode – across all fiber directions (TF, TT, and FT in shear; FF and TT in compression and tension) and across all regions (corpus callosum, corona radiata, basal ganglia, and cortex). The statistical analyses are supposed to indicate which factors should be considered when developing constitutive formulations for human brain tissue.

3. Results

3.1. Pre-conditioning behavior

Fig. 5 shows a representative mechanical response during simple shear, unconfined compression, and tension for a specimen from the corona radiata of brain VIII. The tissue exhibited a nonlinear mechanical response with notable hystereses during cyclic loading. While we observed substantial pre-conditioning between the first and the second loading cycle, pre-conditioning was rather minor during all subsequent cycles. Although the offset of force at zero strain continued to increase for compression and tension (see Fig. 5 b and c), the ‘elastic’ response (average curve between loading and unloading), which we used for calibrating the hyperelastic constitutive model parameters, remained constant.

Fig. 6 shows the stress–stretch response of one specimen from the corona radiata of brain VIII, where we consecutively increased the maximum compressive strain from 0.1 up to 0.4 in steps of 0.1, and performed three cycles per stretch level. The sample displayed marked pre-conditioning during the first cycle of each stretch level, which resulted in a successively softened material response.

Fig. 7 demonstrates the response of a specimen from the corona radiata of brain IX under unconfined compression up to 10% compressive strain when performing two sets of three loading cycles separated by a 60 min recovery period. For this test, we did not glue the sample to the upper specimen holder. This allowed us to slightly lift the upper platform upon completion of the first compression test until platen and specimen were out of contact. Throughout the testing period, we kept the tissue cube surrounded by the droplet of phosphate-buffered saline solution to ensure that the sample did not dry out during the waiting period. Interestingly, after 60 min, the tissue cube had almost completely recovered and showed a pre-conditioning pattern remarkably similar to that of the initial compression test.

3.2. Direction-dependent mechanical behavior

Fig. 8 reveals the influence of anisotropic nerve fiber distribution on the mechanical response in shear, compression, and tension. As nerve fibers are aligned uniaxially in specimens from the corpus callosum, we can distinguish between three possible shear modes and two possible compression and tension modes, as illustrated in Fig. 4. The mean tissue responses showed no significant

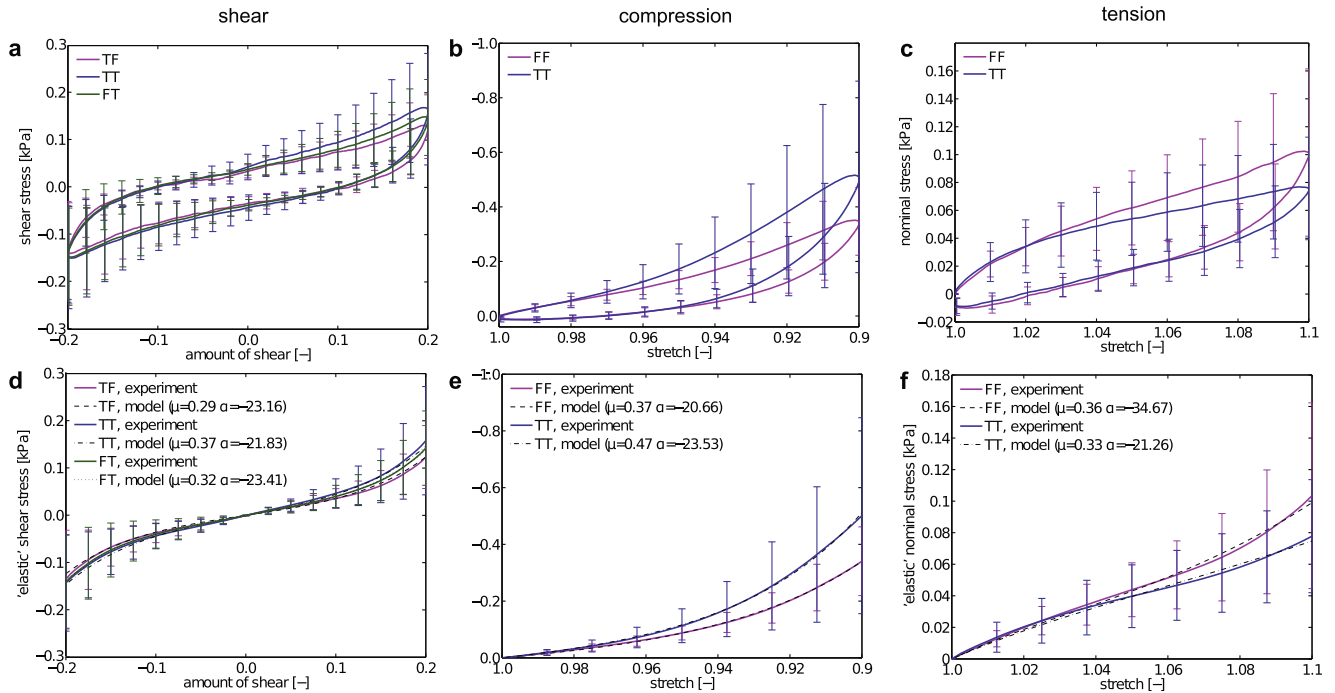


Fig. 8. Direction-dependent behavior of brain tissue: (a)–(c) average curves and corresponding standard deviations indicated by error bars in shear, compression, and tension for specimens from the corpus callosum with different preferred nerve fiber direction. In simple shear, we distinguish between three modes ij , for $ij \in \{T,F\}$, where I denotes the normal vector of the face that is shifted by simple shear and J denotes the direction in which the face is shifted, along (F) or transverse (T) to the uniaxial fiber direction \mathbf{f}_0 . In compression and tension, we distinguish between loading along nerve fibers (FF) and transverse to nerve fibers (TT); (d)–(f) average ‘elastic’ behavior in shear, compression, and tension with corresponding modified Ogden constitutive model with the strain-energy function $\Psi^{\text{Ogd}} = 2\mu/\alpha^2(\lambda_1^\alpha + \lambda_2^\alpha + \lambda_3^\alpha - 3)$. Data reveal no remarkable difference between different shear modes (FT, TT, and TF). In compression, the response was marginally softer in the FF mode. In tension, it was slightly stiffer in the FF mode. The number of specimens considered in shear (s), compression (c), and tension (t) are $n_{s,TF} = 13$, $n_{s,TT} = 13$, $n_{s,FT} = 13$, $n_{c,FF} = 7$, $n_{c,TT} = 13$, $n_{t,FF} = 6$, and $n_{t,TT} = 13$ respectively.

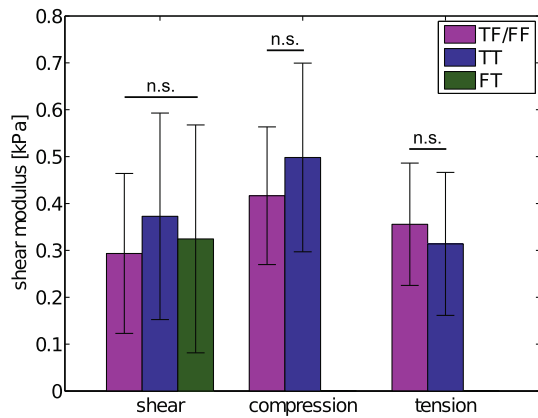


Fig. 9. Column plots of shear moduli (mean \pm SD) obtained from calibrating the modified one-term Ogden model with each experimental curve separately averaged over three possible modes in simple shear (FT, TT, and TF, as denoted in Fig. 4), and two possible modes in compression and tension (FF and TT) for all specimens from the corpus callosum. The data indicate a marginally softer response along nerve fibers in compression and marginally stiffer response along fibers in tension but neither of the differences appeared to be statistically significant.

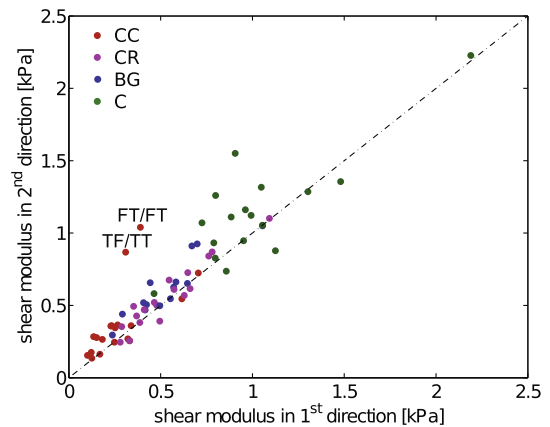


Fig. 10. Shear moduli obtained by calibrating the modified one-term Ogden model with the simple shear response in the first (x -) direction versus shear moduli calibrated with the response in the second (y -) direction, with the line of equality for all tested specimens from the corpus callosum (CC), the corona radiata (CR), the basal ganglia (BG), and the cortex (C) independent of the axon orientation. The results fit a straight line fairly well. Outlying specimens from the corpus callosum, which consist of uniaxially aligned nerve fibers, do not show a correlation between the shear mode (FT, TT, or TF, as denoted in Fig. 4) in the x/y -directions and the anisotropic shear response.

directional dependency. Though, we observed a marginally softer average mechanical response along the fibers (in the FF mode) in compression and a marginally stiffer response along the fibers in tension.

Fig. 8 d–f demonstrate that the modified one-term Ogden model was able to capture the average ‘elastic’ response as the average between the loading and the unloading path in different axon directions for all loading modes. We note that the average between the two paths is assumed to be the hyperelastic tissue behavior as the strain rate approaches zero and the hysteresis vanishes. All

possible shear modes yielded similar values for the material parameters μ and α . In accordance with the slightly stiffer response along fibers in tension, we obtained a slightly higher shear modulus μ for the FF mode than for the TT mode, and a clearly higher value for α . The slightly stiffer response transverse to fibers in compression yielded a higher shear modulus in the TT than in the FF mode.

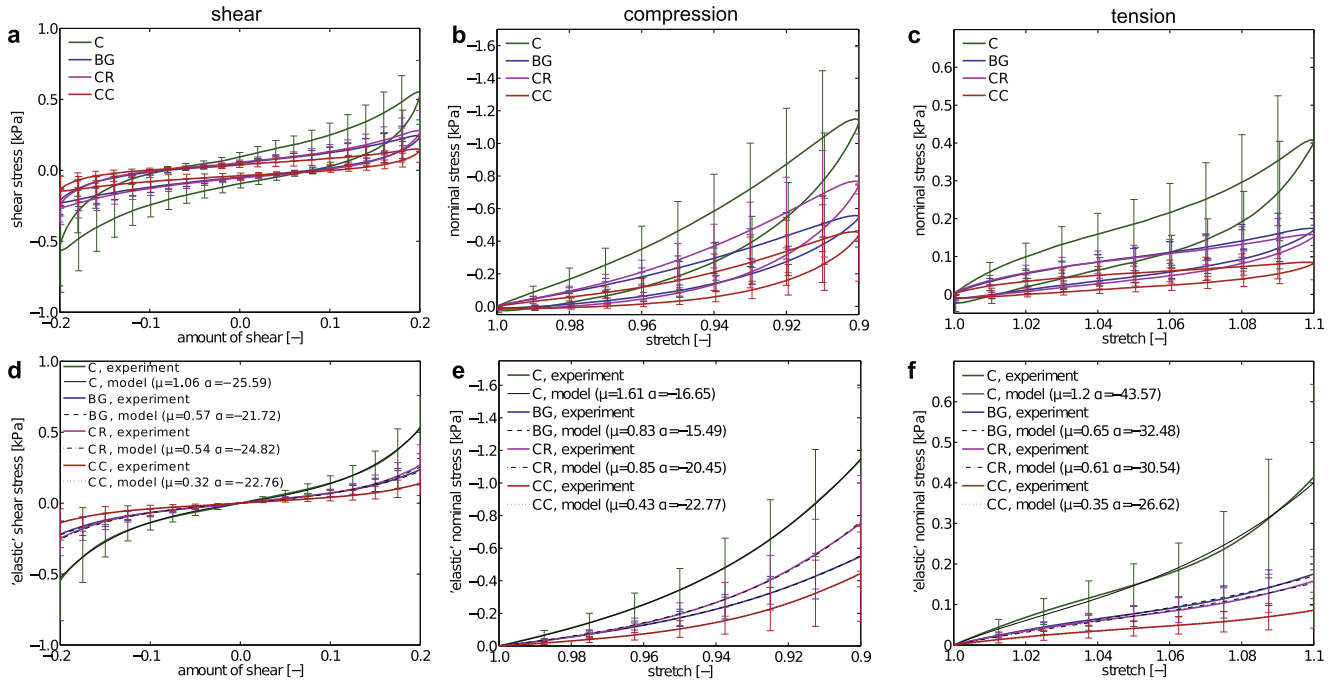


Fig. 11. Region-dependent behavior of brain tissue: (a)–(c) average curves and corresponding standard deviations indicated by error bars in shear, compression, and tension for different regions: corpus callosum (CC), corona radiata (CR), basal ganglia (BG), and cortex (C); (d)–(f) average ‘elastic’ behavior in shear, compression, and tension with corresponding modified Ogden constitutive model with the strain-energy function $\Psi^{Ogd} = 2\mu/\alpha^2(\lambda_1^\alpha + \lambda_2^\alpha + \lambda_3^\alpha - 3)$. The data reveal that the cortex is the stiffest structure, while the corpus callosum is the softest. The mechanical behavior of tissue from the corona radiata and the basal ganglia is similar. The number of specimens considered in shear (s), compression (c), and tension (t) are $n_{s,CC} = 39$, $n_{s,CR} = 36$, $n_{s,BG} = 29$, $n_{s,C} = 35$, $n_{c,CC} = 20$, $n_{c,CR} = 18$, $n_{c,BG} = 15$, $n_{c,C} = 17$, $n_{t,CC} = 19$, $n_{t,CR} = 18$, $n_{t,BG} = 15$, and $n_{t,C} = 15$.

Fig. 9 summarizes the shear moduli (mean \pm SD) obtained by calibrating the modified one-term Ogden model with each experimental curve separately for the three possible modes for simple shear (FT, TT, and TF) and the two possible modes for compression and tension (FF and TT). Neither pairwise *t*-tests nor Tukey–Kramer tests across the different modes revealed statistically significant dependencies on nerve fiber orientation.

Fig. 10 demonstrates directional dependencies in the shear response for all tested specimens – regardless of nerve fiber distribution. In this graph, we plot the shear modulus obtained from calibration with the simple shear response in two orthogonal directions against each other together with the line of equality; each point in Fig. 10 represents one tested tissue cube. The line of equality represents the data fairly well. Although diffusion tensor images confirmed that specimens from the corpus callosum featured the highest anisotropy in terms of their microstructure, rather specimens from the cortex exhibited the highest anisotropy in simple shear experiments. Furthermore, outliers excised from the corpus callosum shown in red do not show a correlation between the anisotropic shear response and the preferred axon orientation. Since we did not find a significant mechanical tissue anisotropy, from now on, we will average the shear response in the *x*- and *y*-directions to obtain a single representative shear response for every tested specimen.

3.3. Region-dependent behavior

Fig. 11 shows the average mechanical response in shear, compression, and tension for the different regions of interest: the corpus callosum, the corona radiata, the basal ganglia, and the cortex. Independent of the loading mode, the cortex exhibited the stiffest behavior and the corpus callosum the softest. The mechanical responses of the corona radiata and the basal ganglia were comparable; the corona radiata was slightly stiffer than the basal ganglia

in shear and compression but slightly softer in tension. This was also reflected by the constitutive parameters obtained from calibrating the modified one-term Ogden model with the average ‘elastic’ response as the average between the loading and the unloading path, as shown in Fig. 11 d–f. The shear modulus μ was highest in the cortex and lowest in the corpus callosum, while the basal ganglia and corona radiata displayed similar shear moduli μ . However, coming along with the slightly stiffer response of specimens from the corona radiata in shear and compression, the value of α accounting for the nonlinearity of the curve adopted a slightly higher value. In general, the shear moduli μ were highest in compression and lowest in shear. In contrast, the α values were highest in tension and lowest in compression. In tension, tissue samples from the cortex exhibited a qualitatively different, particularly nonlinear response, which resulted in a significantly higher value for α .

Fig. 12a displays column plots of the shear moduli (mean \pm SD) obtained from separately calibrating the modified one-term Ogden model with each experimental curve. Pairwise *t*-tests revealed that shear moduli in the cortex were significantly larger and the shear moduli in the corpus callosum were significantly smaller than in all other regions, as denoted by the asterisks in Fig. 12a. However, there was no significant difference between the shear moduli in the corona radiata and the basal ganglia. The Tukey–Kramer tests across all regions confirmed the results of the pairwise *t*-tests in compression; in shear and tension, however, corona radiata and corpus callosum were not significantly different from one another.

Tables 4–6 summarize all shear moduli μ and corresponding α from calibrating the modified one-term Ogden model with each ‘elastic’ response in shear, compression, and tension. Missing entries indicate that some brains did not provide enough tissue to extract the desired number of specimens or that specimens got damaged during testing. We tested the quality of each calibration by evaluating the coefficient of determination with an average

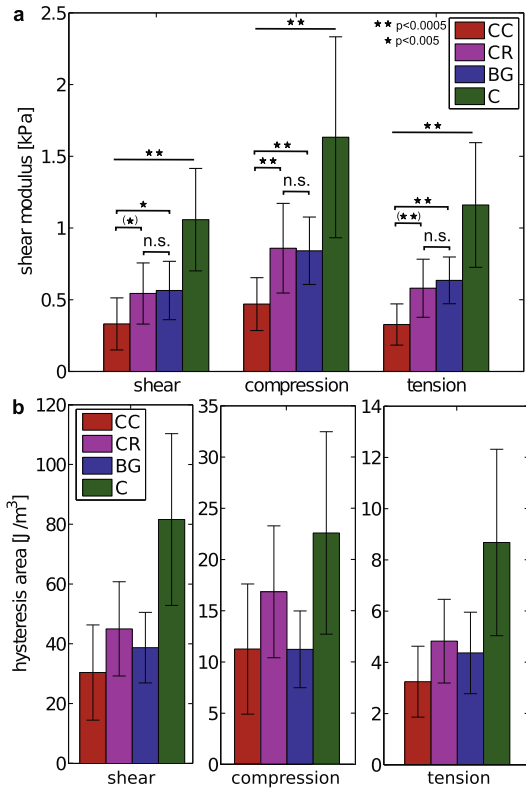


Fig. 12. (a) Column plots of shear moduli (mean ± SD) obtained from calibrating the modified one-term Ogden model with each experimental curve separately averaged over different regions, the corpus callosum (CC), the corona radiata (CR), the basal ganglia (BG), and the cortex (C) in shear, compression and tension. Compression experiments yield higher shear moduli than simple shear and tension experiments. Independent of the loading mode, the cortex was the stiffest structure and the corpus callosum the softest. Asterisks denote statistically significant differences from pairwise *t*-tests; significances in parentheses were not confirmed by Tukey–Kramer tests for multiple comparisons; (b) average hysteresis area (mean ± SD) for different regions (CC, CR, BG, and C) under different loading modes (shear, compression, and tension). The hysteresis area strongly depends on the loading mode and correlates with the applied deformation. White matter exhibits a larger hysteresis area than gray matter.

of $\bar{R}^2 = 0.964$ in shear, $\bar{R}^2 = 0.999$ in compression, and $\bar{R}^2 = 0.990$ in tension. The comparatively low coefficient of determination in shear arises from the fact that the shear responses in the two orthogonal directions were calibrated simultaneously, and that some specimens exhibited a slightly anisotropic shear behavior, as indicated in Fig. 10.

Fig. 12b shows the average hysteresis areas (mean ± SD) as a measure of the dissipated energy during one loading cycle. The hysteresis area strongly depends on the loading mode and correlates with the maximum amount of strain and stress. Under similar loading conditions, specimens from the corona radiata and from the corpus callosum exhibited larger hysteresis areas compared to the corresponding shear moduli shown in Fig. 12a. Accordingly, in contrast to comparisons of shear moduli in different regions, *t*-tests revealed significant differences for all pairwise comparisons besides the corpus callosum and basal ganglia under shear and compressive loading. Tukey–Kramer tests denoted no significant difference between the corona radiata and basal ganglia in shear, and additionally no difference between corona radiata and cortex in compression. In tension, both pairwise *t*-tests and the Tukey–Kramer test revealed that the average hysteresis areas of all regions were significantly different from one another with exceptions of the corona radiata and basal ganglia, similar to the corresponding shear moduli.

3.4. Time-dependent behavior

Fig. 13 a and c show the average scaled stress relaxation and corresponding standard deviations for different brain regions in shear and compression. We averaged the relaxation behavior in shear over all data obtained including two orthogonal directions for each specimen, which leads to a higher number of curves considered in shear than in compression. In tension, the stress recorded during the relaxation period has been too low to provide reasonable results. Column plots (mean ± SD) of the corresponding peak stress (Fig. 13b), and stress relaxation percentage after 5 min (Fig. 13d) indicate that the relaxation behavior did not correlate with the elastic behavior of the tissue. In fact, white matter relaxed faster than gray matter. Within white matter, the corpus callosum appeared to relax faster than the corona radiata, whereas in gray matter, the basal ganglia

Table 4

Constitutive parameters obtained from calibrating the modified Ogden model with the strain-energy function $\Psi^{Ogd} = 2\mu/\alpha^2(\lambda_1^\alpha + \lambda_2^\alpha + \lambda_3^\alpha - 3)$ and the shear response of each tested specimen. The average coefficient of determination was $\bar{R}^2 = 0.964$ with a standard deviation of ± 0.094 . Values are averaged (mean ± SD) over different regions, the corpus callosum (CC), the corona radiata (CR), the basal ganglia (BG), and the cortex (C), and different subjects, brain I–X.

		CC	CC	CC	CR	CR	BG	BG	C	C	mean ± SD
I	μ	0.13	0.22	–	0.40	0.49	0.79	0.60	0.79	1.00	0.55 ± 0.30
	α	–22.4	–17.8	–	–25.7	–25.2	–16.8	–32.5	–33.9	–30.8	–25.7 ± 6.5
II	μ	0.32	0.25	–	0.32	0.61	0.36	0.55	0.88	1.29	0.57 ± 0.36
	α	–17.5	–25.4	–	–34.2	–30.0	–25.7	–19.1	–29.6	–27.7	–26.1 ± 5.6
III	μ	0.47	0.21	0.57	0.82	1.10	0.65	–	1.00	0.81	0.70 ± 0.29
	α	–26.6	–17.5	–26.6	–27.5	–23.7	–24.6	–	–27.9	–21.8	–24.5 ± 3.5
IV	μ	0.71	0.57	–	0.59	0.69	0.46	1.05	–	2.21	0.90 ± 0.61
	α	–19.2	–25.7	–	–28.3	–16.8	–23.7	–17.5	–	–28.2	–22.8 ± 4.9
V	μ	–	–	–	0.49	–	–	–	1.06	–	0.77 ± 0.40
	α	–	–	–	–17.2	–	–	–	–21.0	–	–19.1 ± 2.7
VI	μ	0.29	0.30	0.35	0.60	0.38	0.62	0.81	1.18	1.05	0.62 ± 0.33
	α	–22.8	–15.6	–14.8	–22.4	–13.0	–16.2	–19.6	–21.1	–22.0	–18.6 ± 3.7
VII	μ	0.30	0.29	0.71	0.64	0.80	–	–	1.42	1.22	0.77 ± 0.43
	α	–16.7	–15.2	–17.0	–28.3	–17.1	–	–	–16.8	–24.8	–19.4 ± 5.0
VIII	μ	0.17	0.15	–	0.44	0.29	0.27	0.35	0.86	0.95	0.43 ± 0.31
	α	–21.6	–24.0	–	–18.8	–21.8	–17.5	–19.7	–17.1	–22.0	–20.3 ± 2.4
IX	μ	0.13	0.20	–	0.26	–	0.55	0.44	0.52	1.06	0.45 ± 0.31
	α	–39.6	–23.9	–	–33.3	–	–18.7	–20.8	–27.1	–25.9	–27.0 ± 7.3
X	μ	0.30	–	–	0.44	0.42	0.50	0.46	0.72	1.03	0.55 ± 0.25
	α	–30.0	–	–	–21.6	–24.6	–17.8	–24.0	–21.7	–23.4	–23.3 ± 3.7
Mean	μ		0.33 ± 0.18		0.54 ± 0.21		0.56 ± 0.20		1.06 ± 0.36		
± SD	α		–22.0 ± 6.1		–23.9 ± 5.9		–20.9 ± 4.4		–24.6 ± 4.6		

Table 5
Constitutive parameters obtained from calibrating the modified Ogden model with the strain-energy function $\Psi^{\text{Ogd}} = 2\mu/\alpha^2(\lambda_1^\alpha + \lambda_2^\alpha + \lambda_3^\alpha - 3)$ and the **compression** response of each tested specimen. The average coefficient of determination was $R^2 = 0.999$ with a standard deviation of ± 0.001 . Values are averaged (mean \pm SD) over different regions, the corpus callosum (CC), the corona radiata (CR), the basal ganglia (BG), and the cortex (C), and different subjects, brain I–X.

		CC	CC	CC	CR	CR	BG	BG	C	C	mean \pm SD
I	μ	0.31	0.48	–	0.56	0.67	0.98	0.78	0.86	1.00	0.70 \pm 0.24
	α	48.2	–22.9	–	–24.8	–21.2	–15.1	–18.2	–24.5	–24.1	–12.8 \pm 24.9
II	μ	0.47	0.32	–	0.66	0.85	0.57	1.09	1.29	1.90	0.89 \pm 0.52
	α	–20.3	–23.7	–	–23.7	–15.9	–17.3	–18.8	–16.9	–15.7	–19.0 \pm 3.2
III	μ	0.49	0.36	0.67	1.22	1.23	0.93	–	1.34	0.89	0.89 \pm 0.36
	α	–21.7	–24.3	–25.9	–23.2	–21.1	–13.9	–	–19.7	–19.0	–21.1 \pm 3.7
IV	μ	0.32	0.52	–	1.12	1.44	0.69	1.40	–	2.67	1.17 \pm 0.79
	α	–23.0	–31.2	–	–18.7	–17.0	–19.2	–14.2	–	–10.9	–19.2 \pm 6.5
V	μ	–	–	–	0.95	–	–	–	2.42	–	1.69 \pm 1.04
	α	–	–	–	–23.7	–	–	–	–16.7	–	–20.2 \pm 5.0
VI	μ	0.35	0.56	0.49	0.94	0.73	0.95	0.98	2.77	2.10	1.09 \pm 0.81
	α	–27.1	–22.3	–18.3	–18.5	–16.4	–14.9	–17.8	–12.4	–10.4	–17.6 \pm 5.0
VII	μ	0.29	0.27	1.07	0.91	1.42	–	–	2.17	2.44	1.23 \pm 0.85
	α	–22.4	–23.8	–25.7	–26.2	–15.5	–	–	–12.4	–14.0	–20.0 \pm 5.8
VIII	μ	0.41	0.46	–	0.48	0.55	0.60	0.67	1.42	1.30	0.74 \pm 0.40
	α	34.8	–10.6	–	–17.5	–12.7	29.1	–15.5	–12.7	–12.4	–2.2 \pm 21.2
IX	μ	0.70	0.41	–	0.60	–	0.98	0.66	0.53	1.69	0.79 \pm 0.43
	α	14.2	34.8	–	–22.9	–	–10.8	–13.0	–16.2	–25.9	–5.7 \pm 22.1
X	μ	0.45	–	–	0.61	0.53	0.83	0.52	–	0.95	0.65 \pm 0.20
	α	–17.8	–	–	–17.5	–21.0	–12.4	–15.4	–	–16.1	–16.7 \pm 2.9
Mean	μ		0.47 \pm 0.18		0.86 \pm 0.31		0.84 \pm 0.24		1.63 \pm 0.70		
\pm SD	α		–11.4 \pm 23.8		–19.9 \pm 3.7		–12.5 \pm 11.7		–16.5 \pm 4.8		

Table 6
Constitutive parameters obtained from calibrating the modified Ogden model with the strain-energy function $\Psi^{\text{Ogd}} = 2\mu/\alpha^2(\lambda_1^\alpha + \lambda_2^\alpha + \lambda_3^\alpha - 3)$ and the **tension** response of each tested specimen. The average coefficient of determination is $R^2 = 0.990$ with a standard deviation of ± 0.018 . Values are averaged (mean \pm SD) over different regions, the corpus callosum (CC), the corona radiata (CR), the basal ganglia (BG), and the cortex (C), and different subjects, brain I–X.

		CC	CC	CC	CR	CR	BG	BG	C	C	Mean \pm SD
I	μ	–	0.27	–	0.19	0.50	0.89	0.56	0.83	0.84	0.58 \pm 0.28
	α	–	–15.9	–	–22.6	–34.1	–39.7	–32.9	–82.9	–58.7	–41.0 \pm 22.9
II	μ	0.50	0.33	–	0.42	0.74	0.52	0.52	0.91	1.58	0.69 \pm 0.40
	α	–45.5	–30.9	–	–46.3	–36.7	–45.4	–20.7	–45.4	–55.0	–40.7 \pm 10.8
III	μ	0.48	0.27	0.45	0.83	0.94	0.80	–	0.99	–	0.68 \pm 0.28
	α	–18.4	–12.9	–14.0	–40.5	–37.2	–38.0	–	–38.6	–	–28.5 \pm 12.7
IV	μ	0.21	0.05	–	0.73	0.85	0.43	0.87	–	2.21	0.77 \pm 0.71
	α	–20.9	–73.5	–	–36.4	–11.6	–19.7	–25.9	–	–46.1	–33.4 \pm 21.0
V	μ	–	–	–	0.52	–	–	–	1.27	–	0.90 \pm 0.53
	α	–	–	–	–12.8	–	–	–	–13.4	–	–13.1 \pm 0.4
VI	μ	0.26	0.29	0.27	0.54	0.67	0.61	0.67	1.30	1.47	0.68 \pm 0.44
	α	–20.8	–11.8	–10.0	–29.0	–13.3	–11.8	–17.8	–13.5	–17.2	–16.1 \pm 5.9
VII	μ	0.24	0.20	0.68	0.60	0.78	–	–	–	1.54	0.67 \pm 0.49
	α	–22.8	–12.2	–12.1	–46.1	–12.1	–	–	–	–23.6	–21.5 \pm 13.2
VIII	μ	0.22	0.35	–	0.35	0.56	0.38	0.60	0.84	1.04	0.54 \pm 0.28
	α	–24.2	–15.3	–	–12.6	–30.2	–16.9	–55.5	–12.6	–40.8	–26.0 \pm 15.4
IX	μ	0.43	0.23	–	0.41	–	0.79	0.57	0.50	1.36	0.61 \pm 0.37
	α	–46.1	–36.3	–	–26.0	–	–21.8	–28.5	–57.0	–35.7	–35.9 \pm 12.3
X	μ	0.47	–	–	0.44	0.36	0.82	0.49	–	0.71	0.55 \pm 0.17
	α	–42.3	–	–	–30.9	–47.9	–35.3	–39.5	–	–42.5	–39.7 \pm 6.0
Mean	μ		0.33 \pm 0.14		0.58 \pm 0.20		0.64 \pm 0.16		1.16 \pm 0.43		
\pm SD	α		–25.6 \pm 16.5		–29.2 \pm 12.6		–30.0 \pm 12.2		–38.9 \pm 20.2		

and the cortex exhibited similar relaxation behavior. For shear loading, pairwise *t*-tests revealed that the relaxation percentages after 5 min are indistinguishable in corona radiata and corpus callosum, and basal ganglia and cortex, respectively; both gray matter regions showed a significantly different relaxation behavior from both white matter regions. The Tukey–Kramer test only confirmed differences between corona radiata and cortex and basal ganglia and corpus callosum, respectively. For compressive loading, pairwise *t*-tests indicated significant differences in the relaxation behavior of all pairs of regions besides the basal ganglia and the cortex, which was confirmed by the Tukey–Kramer test.

Fig. 12a reveals that the peak stresses during the relaxation experiments showed different regional trends than the shear moduli in Fig. 12a. For shear loading, pairwise *t*-tests again revealed significantly higher stresses in the cortex than in all other regions, but stresses in the corona radiata were significantly higher than in the basal ganglia and the corpus callosum, while the latter two were indistinguishable. The Tukey–Kramer test confirmed all significant relations besides the one between corona radiata and basal ganglia. For compression loading, peak stresses in cortex and corona radiata showed no significant difference. While the *t*-test still notified significantly higher stresses in the corona radiata than in

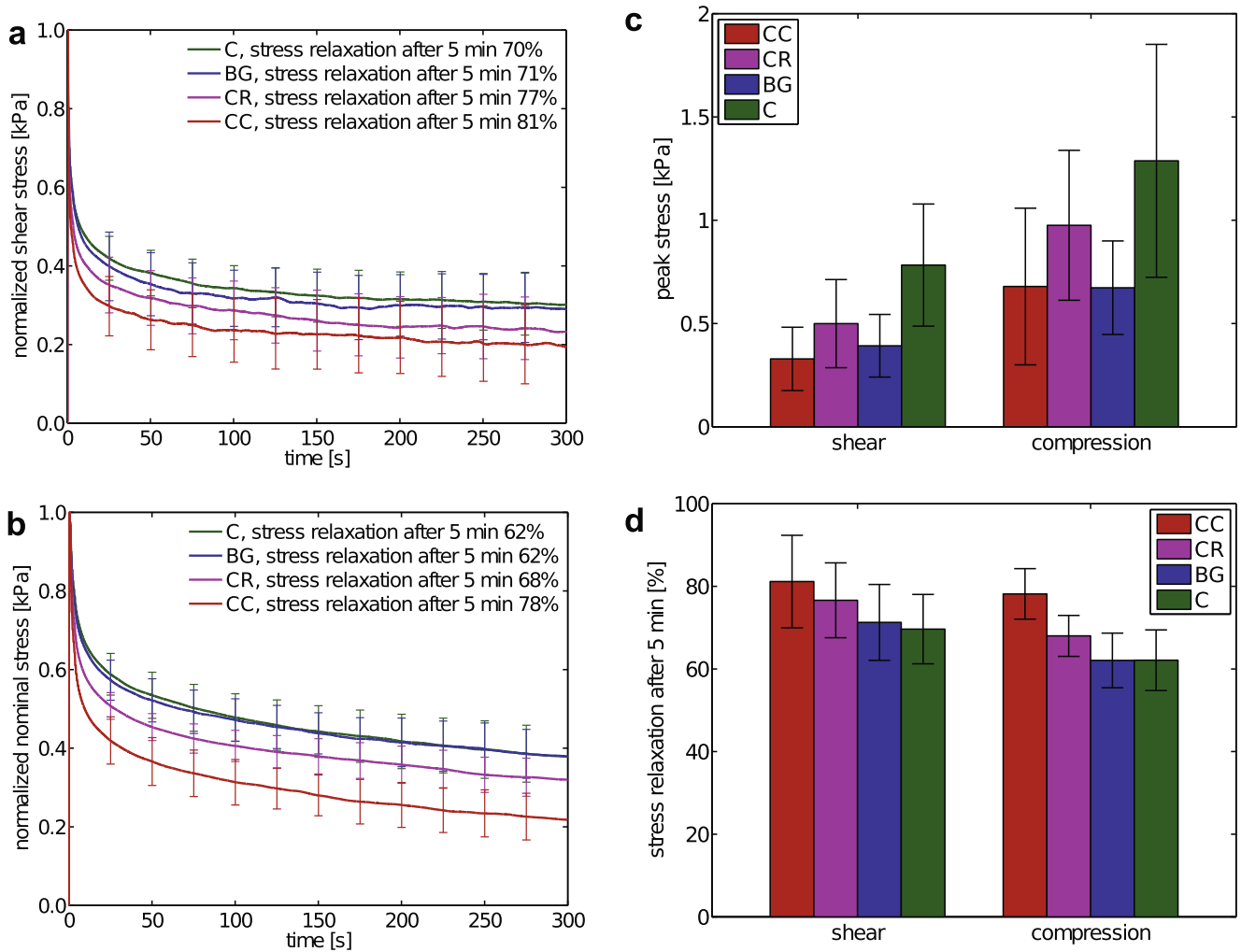


Fig. 13. Time-dependent behavior of human brain tissue: (a) average scaled stress relaxation behavior and corresponding standard deviations indicated by error bars at an amount of shear $\gamma = 0.2$ in different regions of the brain, the corpus callosum (CC; $n = 20$), the corona radiata (CR; $n = 31$), the basal ganglia (BG; $n = 26$), and the cortex (C; $n = 33$); (b) average scaled stress relaxation behavior at 10% compression in the CC ($n = 18$), the CR ($n = 18$), the BG ($n = 15$), and the C ($n = 16$); (c) column plots of peak stresses at an amount of shear of $\gamma = 0.2$ and 10% compression (mean \pm SD) indicate that the elastic behavior does not correlate with the relaxation behavior. The peak stresses were highest in the cortex, intermediate in the corona radiata, and lowest in the basal ganglia and corpus callosum; (d) column plots of the stress relaxation percentages after 5 min (mean \pm SD). White matter (CC and CR) relaxed faster than gray matter (BG and C).

the corpus callosum and the basal ganglia similar to shear loading, the Tukey–Kramer did not.

3.5. Microstructural analysis

Fig. 14 illustrates the microstructure of one representative tissue cube from each region of brain VI, the corpus callosum, the corona radiata, the basal ganglia, and the cortex. The Klüver Barrera staining (Fig. 14 a and b) – coloring myelin wrapped around nerve fibers in blue, neuropil in pink, and nerve cells in purple – reveals a similar cell decomposition in white matter, the corpus callosum and the corona radiata, and in gray matter, the basal ganglia and the cortex, respectively. The stains from the corpus callosum (Fig. 14a left) further confirm the uniaxial orientation of nerve fibers in the corpus callosum, where glial cells shown in purple and pink highly align along axon bundles.

The Gomori silver staining shown in Fig. 14c not only colors cell nuclei but also interconnections including axons and dendrites. This stain evidences the microstructural distinction of all four regions of interest. Cell bodies in the cortex are larger and dendrites are more branched than in the basal ganglia.

To ensure that the microstructure was not altered during biomechanical testing, we additionally fixed and stained tissue

cubes adjacent to the tested regions. The microstructural investigation revealed no indication of changes in the microstructure as a result of the testing protocol: cell bodies had similar size, shape and distribution.

3.6. Calibrating hyperelastic constitutive parameters

Fig. 15 compares the calibrated constitutive models from Section 2.6.4 using the ‘elastic’ experimental data of each loading mode separately (Fig. 15 a–c) with the calibrated models using all loading modes simultaneously (Fig. 15 d–f), here shown exemplarily for measurements of the corona radiata.

Table 7 summarizes the corresponding material parameters and coefficients of determination for all four regions. As the shear response of brain deviated from linearity, even for small amounts of shear, neither the neo-Hookean nor the Mooney–Rivlin constitutive model were able to satisfactorily represent the experimental data, as shown in Fig. 15 d–f. While the Gent, the Demiray, and the modified one-term Ogden model represented the data well when calibrated with each loading mode separately, only the latter was able to represent all loading modes simultaneously. More precisely, only the one-term Ogden model was able to capture the compression-tension asymmetry with a notably softer response

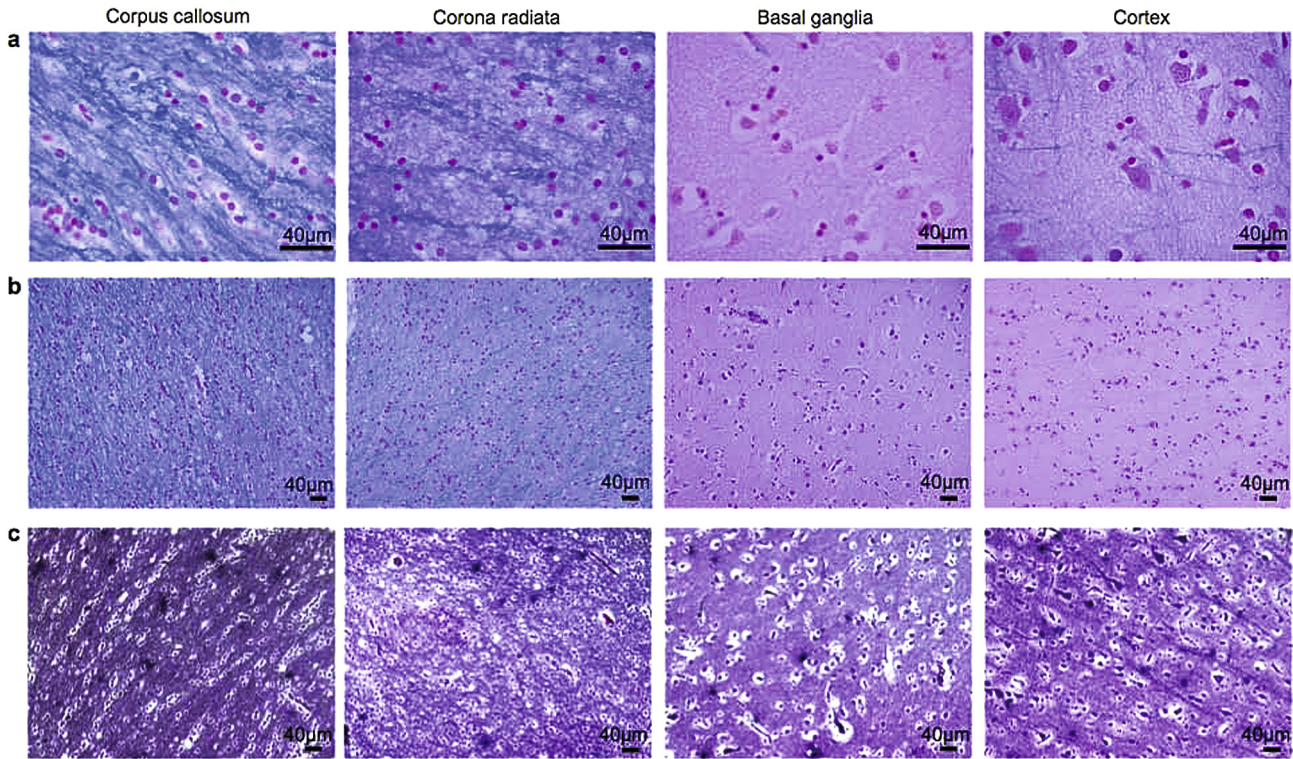


Fig. 14. Microstructure of an exemplary specimen from each region of brain VI, the corpus callosum, the corona radiata, the basal ganglia, and the cortex: (a) Klüver-Barrera staining coloring myelin wrapped around nerve fibers in blue, neuropil in pink, and nerve cells in purple at 63 \times magnification; (b) Klüver-Barrera staining at 20 \times magnification; (c) Gomori silver staining coloring cell nuclei and interconnections including axons and dendrites in brown and black at 20 \times magnification.

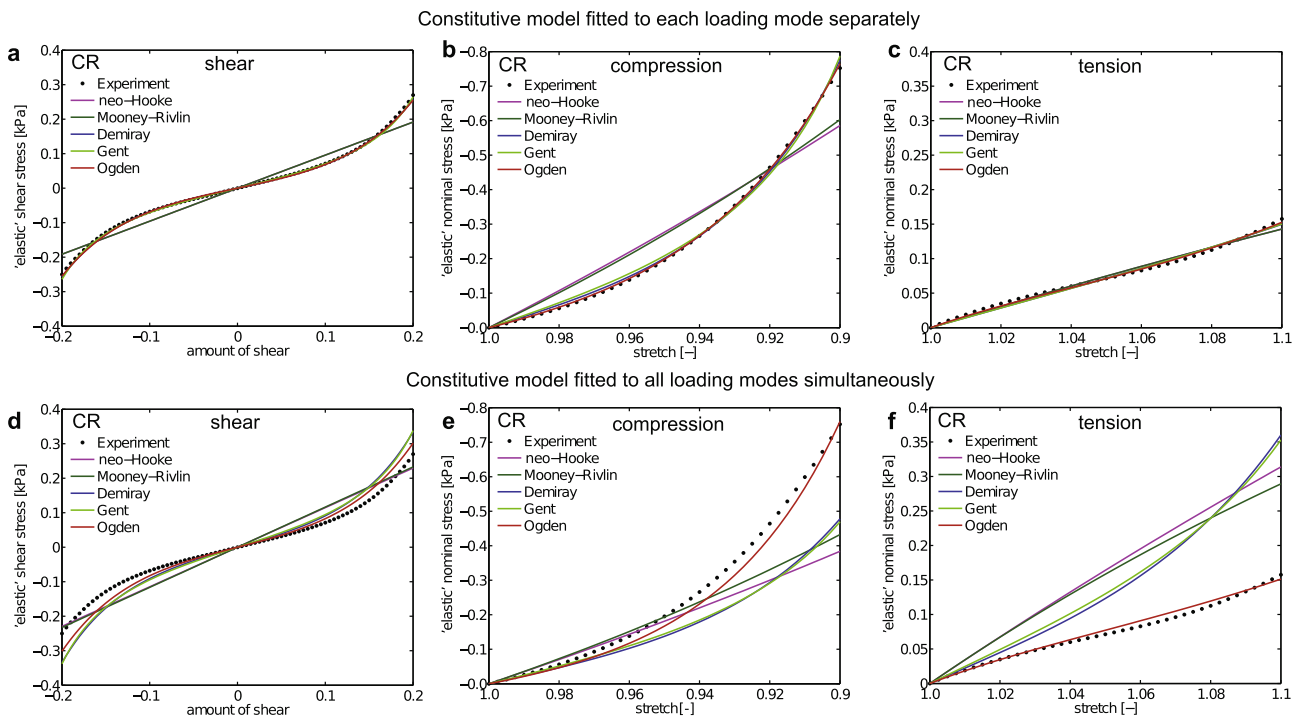


Fig. 15. Calibrating constitutive parameters. Different hyperelastic strain-energy functions (neo-Hooke, Mooney–Rivlin, Demiray, Gent, and Ogden) calibrated with average experimental data for all specimens from the corona radiata (CR) in shear ($n = 36$), compression ($n = 18$), and tension ($n = 18$). Black dots denote experimental data points considered for calibration: (a)–(c) constitutive models calibrated with data from each loading mode separately; (d)–(f) constitutive models calibrated with data from all loading modes simultaneously. The constitutive parameters are given in Table 7. While the Demiray, the Gent and the modified one-term Ogden model satisfactorily represent the response of each loading mode separately, only the modified one-term Ogden model is able to represent the response of all loading modes simultaneously.

Table 7

Constitutive parameters and corresponding coefficients of determination obtained by calibrating five hyperelastic constitutive models (neo-Hookean, Mooney–Rivlin, Demiray, Gent, and modified one-term Ogden model) with the averaged ‘elastic’ behavior in different regions, the corpus callosum (CC), the corona radiata (CR), the basal ganglia (BG), and the cortex (C), for each loading mode separately, and all loading modes simultaneously.

	Shear			Compression			Tension			Simultaneous fit				
<i>neo-Hookean model</i>														
	μ	R^2	μ	R^2	μ	R^2	μ	R^2	μ	R^2	R_c^2	R_t^2	R_s^2	
CC	0.53	0.966	0.99	0.877	0.29	0.988	0.65	0.920	0.608	0.000				
CR	0.96	0.955	1.75	0.900	0.52	0.986	1.15	0.918	0.627	0.000				
BG	0.89	0.970	1.37	0.944	0.57	0.984	0.99	0.957	0.738	0.000				
C	1.95	0.952	2.80	0.935	1.22	0.945	2.07	0.948	0.763	0.000				
<i>Mooney–Rivlin model</i>														
	μ	c_2	R^2	μ	c_2	R^2	μ	c_2	R^2	μ	c_2	R_c^2	R_t^2	R_s^2
CC	0.53	0.13	0.966	0.92	0.00	0.897	0.29	0.13	0.988	0.65	0.00	0.912	0.712	0.000
CR	0.96	0.24	0.955	1.62	0.00	0.919	0.52	0.26	0.986	1.16	0.00	0.911	0.733	0.000
BG	0.89	0.22	0.970	1.27	0.00	0.959	0.57	0.29	0.984	1.00	0.00	0.956	0.834	0.000
C	1.95	0.49	0.952	2.59	0.00	0.951	1.22	0.61	0.945	2.08	0.00	0.948	0.851	0.000
<i>Demiray model</i>														
	μ	β	R^2	μ	β	R^2	μ	β	R^2	μ	β	R_c^2	R_t^2	R_s^2
CC	0.33	18.1	0.999	0.55	28.4	0.999	0.28	1.29	0.988	0.42	20.5	0.883	0.680	0.000
CR	0.56	20.8	0.999	1.05	24.6	0.998	0.48	4.37	0.990	0.74	20.3	0.905	0.688	0.000
BG	0.58	16.6	0.999	0.97	17.1	0.999	0.52	6.03	0.992	0.71	15.8	0.962	0.774	0.000
C	1.17	21.9	1.000	1.90	18.8	0.999	0.91	16.7	0.992	1.35	20.0	0.975	0.809	0.000
<i>Gent model</i>														
	μ	η	R^2	μ	η	R^2	μ	η	R^2	μ	η	R_c^2	R_t^2	R_s^2
CC	0.36	0.08	1.000	0.62	0.06	0.995	0.29	85.0	0.988	0.46	0.08	0.887	0.671	0.000
CR	0.62	0.08	0.999	1.16	0.06	0.995	0.48	0.23	0.990	0.82	0.08	0.907	0.680	0.000
BG	0.62	0.09	0.999	1.01	0.08	0.998	0.52	0.18	0.992	0.75	0.09	0.962	0.771	0.000
C	1.23	0.07	1.000	2.01	0.08	0.998	0.92	0.08	0.994	1.47	0.08	0.975	0.804	0.000
<i>Modified one-term Ogden model</i>														
	μ	α	R^2	μ	α	R^2	μ	α	R^2	μ	α	R_c^2	R_t^2	R_s^2
CC	0.32	-22.8	0.999	0.43	-22.8	1.000	0.35	-26.6	0.995	0.35	-25.3	0.947	0.988	0.994
CR	0.54	-24.8	0.999	0.85	-20.5	1.000	0.61	-30.5	0.996	0.66	-24.3	0.962	0.986	0.986
BG	0.57	-21.7	0.998	0.83	-15.5	1.000	0.65	-32.5	0.997	0.70	-18.7	0.989	0.993	0.980
C	1.06	-25.6	0.999	1.61	-16.6	1.000	1.20	-43.6	0.996	1.43	-19.0	0.991	0.998	0.928

in tension than in compression by adopting a negative value for the material parameter α . In general, unconfined compression overestimated the stiffness values, while shear and tension underestimated the stiffness compared to the values obtained from the simultaneous calibration with all loading modes. Especially for tissue from the basal ganglia and the cortex, the absolute value of the parameter α , which accounts for the nonlinearity of the stress–strain response, was higher in tension than in shear and compression. We note that in simple shear, shear stresses predicted by the constitutive model are independent of the sign of α . Thus, calibrating the constitutive model exclusively with simple shear data does not provide information on the sign of the parameter α .

3.7. Combined loading

Fig. 16a shows the average shear stress versus amount of shear behavior of specimens from the corona radiata with the corresponding standard deviations indicated by error bars for all axial stretch levels performed under combined compression/tension–shear loading according to protocol 2. Consistent with the compression–tension asymmetry observed during protocol 1, shear stresses increased with increasing compression but remained almost constant with increasing tension. Fig. 16b illustrates that the modified one-term Ogden model, Eq. (12), was able to capture this feature with an average coefficient of determination of $R^2 = 0.966$. Calibrating the constitutive model with the average ‘elastic’ response of all axial stretch levels simultaneously yielded a similar value for the shear modulus μ as calibrating the model with the average experimental data in the corona radiata of all

loading modes in protocol 1 simultaneously, as indicated in Table 7, bottom. However, the absolute value of α obtained from protocol 2 was much lower than the corresponding value obtained from protocol 1. A high value of $\alpha \sim -20$ would yield unrealistically high shear stresses for high compressive or tensile pre-strain in the combined loading case. In contrast, a low value of $\alpha \sim -7$ is not capable of representing the nonlinearity of the shear stress versus amount of shear curve reasonably well.

3.8. Magnetic resonance imaging

Fig. 2d shows an RGB color-coded FA image, where FA is represented by the intensity (brightness), and the color encodes the orientation of the eigenvector associated with λ_1 , by mapping its three elements to the RGB color space.

Correlation of FA with the shear moduli μ showed a linear dependency with a negative slope in shear ($\mu = 1.18 - 1.34$ FA, $r = -0.65$, $p < 0.001$), compression ($\mu = 1.84 - 2.17$ FA, $r = -0.65$, $p < 0.001$), tension ($\mu = 1.3 - 1.55$ FA, $r = -0.69$, $p < 0.001$) and under simultaneous loading ($\mu = 1.57 - 1.96$ FA, $r = -0.66$, $p < 0.001$). The strongest decrease of μ with increasing FA was found in compression, which is shown in Fig. 17. The correlation shown in Fig. 17 is similar for shear, tension and simultaneous loading.

4. Discussion

The current experimental study provides not only novel insights into regional and directional variations of brain tissue

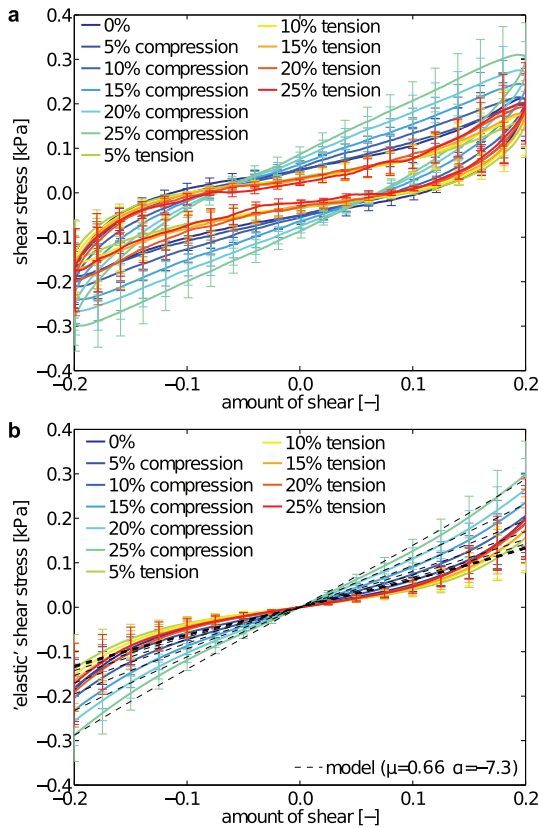


Fig. 16. Combined compression/tension-shear loading: (a) average shear stress versus amount of shear response; (b) average 'elastic' shear stress versus amount of shear with standard deviations indicated by error bars and corresponding model fit to the modified Ogden strain-energy function $\Psi^{\text{Ogd}} = 2\mu/\alpha^2(\lambda_1^{\alpha} + \lambda_2^{\alpha} + \lambda_3^{\alpha} - 3)$ for sinusoidal simple shear superimposed on axial stretch $\lambda = 1.0$ ($n = 8$), 0.95 ($n = 8$), 0.9 ($n = 8$), 0.85 ($n = 8$), 0.8 ($n = 8$), 0.75 ($n = 8$), 1.05 ($n = 8$), 1.1 ($n = 8$), 1.15 ($n = 8$), 1.2 ($n = 8$), and 1.25 ($n = 5$). The average coefficient of determination was $R^2 = 0.966$ with a standard deviation of ± 0.026 . Shear stresses increase with increasing compressive strain but not with increasing tensile strain.

properties, but also essential information to establish realistic constitutive models capable of capturing the mechanics of the brain under multiaxial loading. For the first time, we tested the same specimen under different loading modes, simple shear in two orthogonal directions, unconfined compression, and extension, and performed complementary combined compression/tension-shear tests. Furthermore, we combined biomechanical testing with antecedent diffusion tensor imaging and histological staining. In agreement with previous studies [37,18], we observed that the mechanical response of human brain tissue is highly nonlinear and viscoelastic, with a pronounced compression-tension asymmetry. The elastic response is region-dependent but not direction-dependent, not even in the microstructurally highly anisotropic corpus callosum. The viscous response is also regional-dependent. Of all five models analyzed in our study, neo-Hookean, Mooney Rivlin, Demiray, Gent, and Ogden, only the isotropic modified one-term Ogden model is capable of representing the hyperelastic tissue response under combined shear, compression, and tension loadings. It captures the significantly stiffer response in compression than in tension, and the characteristic increase in shear stress under superimposed compression, but not under superimposed tension.

4.1. Pre-conditioning behavior

During cyclic loading, brain tissue exhibited pronounced pre-conditioning effects, as illustrated in Fig. 5. The main part of the

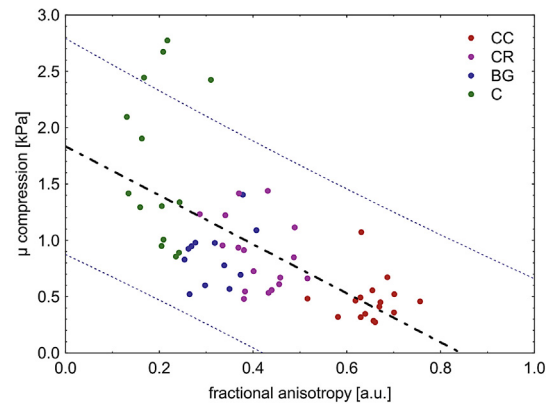


Fig. 17. Correlation of the shear modulus μ under compression with fractional anisotropy FA of all brain samples. There is a significant decrease of the shear modulus with increasing FA ($\mu = 1.84 - 2.17 \text{ FA}$, $r = -0.65$ and $p < 0.001$).

mechanical softening associated with decreasing hysteresis area occurred between the first and second loading cycles. A similar behavior has been reported previously in unconfined uniaxial compression tests of porcine brain tissue [57]. Our experiments revealed that the percentage loss in hysteresis area between the first and second cycles was higher in compression and tension than in shear. Past the second loading cycle, pre-conditioning effects became minor and were mainly characterized by a slight increase in the offset of force at zero strain. We attribute this characteristic to the porous nature of the tissue, where interstitial fluid is gradually squeezed out of the tissue sample. After the first loading cycle, the 'elastic' response remained remarkably constant. To ensure repeatable and comparable results, we decided to perform two pre-conditioning cycles per loading mode. The same number of pre-conditioning cycles has previously been considered as suitable for experiments on porcine brain tissue [15].

The pre-conditioning behavior occurred whenever the tissue was loaded under a new mode and whenever the load increased beyond its previous maximum value. Thereby, the second shear test in the direction orthogonal to the initial one revealed a similar pre-conditioning behavior and similar shear stresses as during primary loading. This observation confirms that we can sequentially load a single sample under different modes and different loading directions without destroying the tissue integrity and altering its mechanical response. When we incrementally increased the applied load, e.g., the compressive strain, as shown in Fig. 6, we observed significant softening during the first cycle of each strain level. Similar strain softening has previously been reported in the passive human myocardium [45].

Our results suggest that the pre-conditioning in brain tissue is recoverable. When repeating an unconfined compression test after a waiting period of one hour, the tissue had fully recovered and displayed a similar pre-conditioning behavior as during the initial test with the same amount of energy dissipation between the first and second cycles and only minor pre-conditioning effects during subsequent cycles, as indicated in Fig. 7. We conclude that the pre-conditioning behavior of brain tissue is not associated with tissue damage such as a microstructural reorganization but with recoverable changes in the tissue state such as drainage of interstitial fluid or intracellular interaction between cytoplasm, nucleus, and membrane during cellular deformation [58]. Our results agree well with comparable experiments performed on porcine brains [57].

4.2. Direction-dependent mechanical behavior

While MRI demonstrated highly anisotropic diffusion properties, our study suggests that white matter tissue is not significantly

anisotropic from a mechanical point of view, especially when compared to other well-characterized soft tissues such as arteries [59]. To deliberately assess mechanical directional dependencies correlated with anisotropic nerve fiber distribution, we performed diffusion tensor imaging prior to biomechanical testing. Of all four regions, we could only specify a distinct fiber orientation in the corpus callosum and, thus, only considered those specimens to ascertain whether an anisotropic fiber orientation on the microscopic scale translates into an anisotropic stiffness distribution on the macroscopic scale. Previous studies had estimated fiber orientations from anatomical studies and used tissue from both the corpus callosum and the corona radiata, combining both regional and directional variations. In addition to the reliable determination of nerve fiber distributions via diffusion tensor imaging, the design of the current study allowed us to assess loading-mode specific contributions of fibers and to minimize the effect of inter-specimen, regional variations.

Interestingly, we observed no significant mechanical directional dependency under any loading mode, even in the microstructurally highly anisotropic corpus callosum. This seems to suggest that nerve fibers are primarily functional elements of our brain that only marginally contribute to its mechanical strength. Mean stresses along fibers appeared slightly higher than perpendicular to the fibers under tensile loading and slightly lower under compressive loading.

For our study, the directional stiffness variation was insignificant, and we conclude that human brain tissue is nearly isotropic. This is consistent with previous reports on bovine [60] and porcine [31] brain tissues and becomes especially important when developing constitutive models for computational simulations. When shearing the same tissue sample in two orthogonal directions, we found similar shear moduli independent of the brain region and fiber distribution, as shown in Fig. 10. Counterintuitively, in shear, we observed the highest directional variation for specimens from the cortex, which exhibit a nearly isotropic microstructure compared to the microstructurally highly anisotropic specimens extracted from the corpus callosum. Due to the ultrasoft and sticky nature of brain tissue, however, we cannot obviate that some outliers (see Fig. 10) might as well be attributed to asymmetric mounting or unintended influences of adhesion or hydration.

Our results agree well with an early study on the rheological shear response of human brain tissue [14], which showed higher directional variation in gray matter than in white matter, but neither of the differences appeared significant. A more recent study confirmed no significant directional dependency of human brain tissue under compressive and tensile loading, but reported significantly higher shear stresses in fiber direction than transverse to fibers [18]. The latter finding may be attributed to the relatively small sample size of four specimens per loading mode and direction. In view of the high inter-specimen variation generally observed for brain tissue and the fact that each specimen was only loaded under a single direction, the observed trend might have evened out for a larger sample size.

In porcine brain tissue, studies found a significantly stiffer shear response orthogonal to nerve fibers than along fibers in the corpus callosum [15]. In the corona radiata, however, the trend was opposite. The authors sheared each specimen in two orthogonal directions similar to our experiments, but only estimated fiber orientation from anatomical knowledge and used rectangular specimen dimensions of $10 \times 5 \times 1$ mm. We noticed that the measured shear stresses were consistently higher in the direction of the longer edge corresponding to the direction orthogonal to fibers in the corpus callosum, and to the fiber direction in the corona radiata. This might indicate that directional dependencies resulted from an unanticipated influence of noncuboidal specimen dimensions rather than from the anisotropic distribution of nerve fibers,

which could explain the contradictory results. Other studies on the porcine corpus callosum found opposite trends with a significantly stiffer response in the fiber direction than perpendicular to it in dynamic shear [17] and tensile tests [16]. In both studies, specimens were relatively large with dimensions of up to $16 \times 16 \times 3$ mm and $5 \times 5 \times 60$ mm. Our diffusion tensor images showed that even in the much larger human brain, it would be challenging to extract specimens of that size that exhibit a sufficiently uniform microstructure.

4.3. Region-dependent behavior

We found that the mechanical behavior of human brain tissue is region-specific. Specimens extracted from the cortex showed the stiffest mechanical response for all loading modes, while specimens from the corpus callosum showed the softest response, as illustrated in Fig. 11. Corona radiata and basal ganglia responded similarly, exhibiting marginal differences depending on the loading mode; tissue from the corona radiata yielded higher stresses in shear and compression but marginally lower stresses in tension. When calibrating the modified one-term Ogden model, differences between corona radiata and basal ganglia were only reflected in the parameter α accounting for the nonlinearity of the stress-strain curve but not in the shear modulus μ . Accordingly, shear moduli in the corona radiata and basal ganglia were statistically indistinguishable, whereas the cortex yielded significantly higher and the corpus callosum significantly lower shear moduli, as summarized in Fig. 12a. In agreement with our findings, previous studies reported no significant difference between human brain tissue from corona radiata and thalamus in dynamic shear tests [14,21]. The visible and functional differences between gray and white matter do not seem to translate markedly to the elastic mechanical response of human brain tissue. Whereas cortical gray matter exhibited a stiffer response than all other regions, internal gray matter excised from the thalamus or the basal ganglia showed a similar response as white matter from the corona radiata. Interestingly, the corpus callosum was the most fragile brain region, which supports the common notion that it is most vulnerable to diffuse axonal injury [61,62]. Our results suggest that this is not only caused by its high exposure to shear forces, but also by its softest, most injury-prone constitutive response.

Due to the limited availability of human brain tissue, the *ex vivo* regional properties have also been assessed in porcine and bovine brains. Rapid stress relaxation tests on porcine brain tissue yielded similar regional inhomogeneities as our experiments [15]; basal ganglia, thalamus and corona radiata were statistically indistinguishable, while the corpus callosum yielded the lowest average shear moduli. On the contrary, one study reported a lower stiffness for gray matter than for white matter, and within the latter a higher shear modulus for the corpus callosum than for the corona radiata under tensile loading [16]. These discrepancies can again be attributed to the large specimen dimensions of 4–6 cm. These large specimens may have included tissue from surrounding structures that might have influenced the results.

Recently, differences in the mechanical response of gray and white matter have also been investigated using nanoindentation testing. White matter was found to be stiffer than gray matter in bovine [26,28] and lamb [17] brains, but the opposite trend was measured in the rat cerebrum, the rat cerebellum [25], and the mouse spinal cord [63]. Those discrepancies may be explained by the highly complex properties of brain tissue, where both time and length scales significantly influence the results (see Sections 4.4 and 4.5).

Recently, magnetic resonance elastography has enabled the study of regional properties of human brain tissue *in vivo*. While some studies found cortical gray matter to be stiffer than white

matter in agreement with our results [24], others reported the opposite trend [23,64]. Contrary to our results, a recent study found a greater stiffness for the corpus callosum than for the corona radiata [27]. However, those results highly depend on the method used to extract elastic properties, and the excitation frequencies. It remains to be shown that *in vivo* magnetic resonance elastography can accurately quantify regional mechanical properties, especially in thin structures such as the cortex and the corpus callosum [65].

4.4. Time-dependent behavior

Our relaxation experiments support the common notion that the response of brain tissue is extremely time-dependent, with a stress relaxation of up to 80% within only 300 s. Viscous relaxation was similar for both white matter regions, corpus callosum and corona radiata, and both gray matter regions, basal ganglia and cortex, as summarized in Fig. 13a, b and d. Within white matter, specimens from the corpus callosum were more viscous than specimens from the corona radiata, with a stress relaxation after five minutes of $\sim 80\%$. Stress relaxation percentages were slightly higher in shear than in compression but both loading modes showed similar regional dependencies. These rheological differences were also reflected in the energy dissipated during each loading cycle, which we quantified by the hysteresis areas of Fig. 12b. Hysteresis areas were larger for white matter than for gray matter specimens relative to the recorded tissue stresses. These observations are consistent with nanoindentation experiments on bovine brain tissue, showing that white matter is more viscous than gray matter [26,28].

When comparing the maximum stresses during quasi-static experiments in Fig. 11 a and b with the peak stresses during stress relaxation experiments in Fig. 13c, it becomes apparent that regional variations in tissue stresses are strain-rate dependent. This is caused by the rheological difference between gray and white matter. In the slow-loading-rate regime, the cortex yields highest and the corpus callosum lowest stresses, while corona radiata and basal ganglia exhibit a similar response. In the fast-loading-rate regime, the corona radiata and corpus callosum have stiffened relative to gray matter and regional trends have shifted towards those of hysteresis areas in Fig. 12b. Notably, in contrast to many existing studies, all our graphs show data from the same specimens. In agreement with these findings, the study [18], loading specimens at a velocity of $v = 150$ mm/min and higher, reported significantly higher stresses in the corona radiata than in all other regions, whereas basal ganglia and corpus callosum showed a statistically indistinguishable response. Contrary to our study, however, the authors found tissue from the cortex to be softer than tissue from the corona radiata. This may be attributed to a specimen size of $14 \times 14 \times 5$ mm, which suggests that specimens from the cortex did not merely include cortical but additionally subcortical white matter, and thus showed a softer response compared to our experiments.

4.5. Microstructure

To explore potential correlations between the macroscopic mechanical response and the underlying microstructure, we fixed each specimen upon completion of biomechanical testing for histological investigations. Klüver-Barrera stains of representative tissue samples from each region in Fig. 14 a and b show that the cellular decomposition is similar in both gray and white matter regions. While the viscous behavior seems to be closely related to this microstructural architecture, the elastic behavior is not. All white matter tissues appeared more viscous than gray matter in Fig. 13. This reflects the network properties similar to filled elas-

tomers [37] and might also be correlated with a lower water content of about 0.71 g/ml in white matter compared to 0.83 g/ml in gray matter [66].

Considering the elastic properties of the tissue, white matter from the corona radiata and gray matter from the basal ganglia yielded similar shear moduli, while the cortex was significantly stiffer and the corpus callosum significantly softer than all other regions. Our results indicate that it is not merely the density or decomposition of cell nuclei or the contribution of nerve fibers that control the elastic response of human brain tissue. Alternatively, we speculate that interconnections and capillary density significantly contribute to the mechanical strength of the tissue. The differences in interconnections in the considered brain regions become apparent through the Gomori silver stain in Fig. 14c. Furthermore, local capillary density and brain activity are not correlated with the density of cell nuclei [67]. In fact, the capillary density appears to develop according to local functional demands [67] and is lowest in the corpus callosum [68]. This could explain why the cortex with high metabolic demands is the stiffest, whereas the corpus callosum is the softest brain region. This hypothesis could also explain why we observe high stiffness variations in tissue from the cortex where vascular patterns are highly region-specific [68].

The correlation between the mechanical properties of nervous tissue and its underlying microstructure has recently been investigated by combining indentation experiments with histological staining. A recent study reported that the stiffness of the mouse spinal cord strongly correlates with the areas of cell nuclei and the cellular in plane proximity [63]; another study revealed that the stiffness of bovine white matter increases with myelin content [29]. Myelin is colored blue in our histological stains in Fig. 14 a and b. Our study suggests that it is primarily the capillary density that explains regional stiffness variations. This could also explain why nanoindentation experiments record a higher stiffness variation in white matter [17,26,28], while quasi-static compression, tension and shear experiments as well as atomic force microscopy indentation [63] record a higher stiffness variation in gray matter. In comparison to indentation tests of intact brain slices, our unconfined tension and compression tests of small tissue samples might very well probe primarily the solid skeleton rather than the overall tissue. Overall, it remains challenging to fully understand the highly complex mechanical response of brain tissue, which significantly depends on time and length scales of the mechanical tests [69].

4.6. Influence of age and gender

Our experimental study neither showed a dependence of brain tissue properties on gender nor on age which can be extracted from Tables 1 and 4–6. We note, though, that our study was limited to tissue samples of 54 to 81 years of age at death. A potential correlation between brain tissue stiffness and brain activity, as indicated in Section 4.5, further impedes the detection of an age-dependency within this limited range as most probably brain activity highly varied between subjects. We anticipate that a larger age window could still reveal age-dependent properties. For example, studies have shown that human brain tissue undergoes a significant increase in stiffness of about 200% between 5 and 22 months of age. The adult brain at ages similar to the age of our subjects appears to be three to four times stiffer than the brain of young children [21].

4.7. Calibrating hyperelastic constitutive parameters

One of the most important results of our study is the side-by-side comparison of different constitutive models for human brain

tissue under multiple loading modes. We explored and calibrated the five most commonly used isotropic strain-energy functions, neo-Hookean, Mooney–Rivlin, Demiray, Gent, and modified one-term Ogden [46]. Our results demonstrate that the material parameters identified for a single loading mode do not necessarily predict the response under different loading conditions [39].

Both the neo-Hookean and the Mooney–Rivlin models assume a linear shear response and, thus, are not eligible to capture the non-linear shear response of human brain tissue, which deviates from linearity already at strains greater than 0.1% [31]. While the Demiray, the Gent, and the modified one-term Ogden models represent the experimental data well when calibrated with each loading mode separately, only the modified one-term Ogden model is able to capture the compression-tension asymmetry when calibrated with all loading modes simultaneously (see Fig. 15). Of all five models, only the modified one-term Ogden model with a strain-energy function of $\Psi^{\text{Ogd}} = 2\mu(\lambda_1^\alpha + \lambda_2^\alpha + \lambda_3^\alpha - 3)/\alpha^2$ is capable of representing the response of human brain tissue under arbitrary loading cases. Its region-specific parameters are summarized in Table 7. We emphasize that the parameter α needs to adopt a negative value to represent the effect that stresses are higher in compression than in tension. A positive value for α would yield the opposite trend, which is inappropriate for brain tissue. This information must be kept in mind when calibrating the one-term Ogden model with shear data only. The shear stresses are independent of the sign of α and minimizing procedures might misleadingly yield a positive value for α .

Our results demonstrate that in comparison to a simultaneous calibration of all loading modes, individual compression experiments overestimate the shear modulus μ , while shear and tension experiments underestimate μ . This agrees with previous studies which report that constitutive models based on experimental data collected in compression are inadequate to explain porcine tissue behavior in tension [39]. Our results show that, among all loading modes, tensile testing yielded shear moduli closest to those of a simultaneous calibration with all loading modes. Notably, the situation was different for the parameter α accounting for the nonlinearity of the stress–strain curve; tension experiments overestimate α , while compression experiments underestimate α . The value obtained from a simultaneous calibration with all loading modes lies in between with $\alpha \sim -20$. White matter exhibited larger nonlinearities associated with higher absolute values for α than gray matter in compression, while we observed the opposite trend in tension.

Our observations are consistent with several studies in the literature. Considering a single loading mode, a recent series of studies has found excellent agreement between experimental data of mixed porcine brain tissue and Demiray, Gent, and Ogden strain-energy functions [40–42]. In conjunction with our results, their compression experiments [40] yielded higher shear moduli than shear and tension experiments [41,42]. Their shear moduli are overall marginally higher than ours, but were also derived from significantly higher strain rates with velocities of 9.000 mm/min compared to 2 mm/min in the present study. Studies that consider only a single loading mode misleadingly yielded positive values for α , with $\alpha \sim 6$, and are, thus, not sufficient to accurately identify the full set of material parameters. Similarly, several studies found an excellent agreement between indentation data and polynomial, Yeoh, and one-term Ogden strain-energy functions using inverse finite elements analysis [47]. Their shear modulus μ lies in the range of our results with a mean of $\mu = 0.624$ kPa in white matter, but again the limitation to a single loading mode leads to an unrealistically positive value of α (~ 18).

All studies in the literature that considered both compression and tension experiments, reported that only the one or two-term

Ogden models could satisfactorily represent the material response [16,37,39]. These studies proposed $\mu = 1.0$ kPa from cyclic compression-tension experiments on human white matter tissue [37], $\mu = 0.8$ kPa and $\alpha = -4.7$ for mixed porcine brain tissue [39], and $\mu = 0.3 - 0.7$ kPa and $\alpha = -7.0$ when extrapolating tensile porcine white matter data to compression [16]. The lower absolute values for α in the literature can be attributed to higher strains of 30% and more, compared to strains of up to 10% in compression and tension, and 20% in shear for the current study.

Only a single study has calibrated hyperelastic constitutive models for all three loading modes: shear, compression, and tension [48]. The authors compared three strain-energy functions implemented in the commercial software ABAQUS, hyperfoam, Ogden, and polynomial, within a finite element model. However, the underlying experimental data were collected at high loading rates, where each specimen was only loaded once up to fairly large strains of 50% without pre-conditioning and only the loading curve was recorded [18]. Thus, it remains questionable whether those experiments are suitable to quantify the hyperelastic response of the brain tissue. Furthermore, the reported parameters fail to satisfy consistency with the linear theory and are, therefore, not readily comparable to the results presented here.

4.8. Combined loading

In addition to a sequence of multiple loading modes, we conducted combined compression/tension-shear tests to critically examine the validity of five commonly used hyperelastic constitutive models and to identify the corresponding material parameters for multiaxial loading cases. Our experiments show that shear stresses increase significantly with increasing superimposed axial compression but only slightly with increasing axial tension. This behavior is the logical outcome of the compression-tension asymmetry of human brain tissue. A similar behavior has previously been observed in oscillatory shear experiments on mouse brain tissue [44], where complex shear moduli increased with increasing compressive strain in the direction orthogonal to shear but remained almost constant with increasing tensile strain. Again, only one of the strain-energy functions considered in this study, the modified one-term Ogden model, can capture this characteristic response of brain tissue [53].

As only the largest region, the corona radiata, provided enough space to extract additional specimens, Fig. 16 represents the average response of tissue from this one white matter region under combined loading conditions. However, during protocol 1, some specimens, especially from the cortex and the basal ganglia, showed a much less pronounced compression-tension asymmetry with higher-than-average tensile stresses. In these cases, we would expect a qualitatively different behavior, in which shear stresses not only increase under increasing compressive strain, but also under increasing tensile strain.

Notably, calibrating the modified one-term Ogden model with average shear stresses recorded for all axial stretch levels, $\lambda = 1.00, \dots, 0.75$ and $\lambda = 1.05, \dots, 1.25$ in steps of 0.05, simultaneously, yields the exact same value for the shear modulus $\mu = 0.66$ kPa as a calibration with multiple uniaxial loading modes, as summarized in Table 7. The parameter α , in contrast, adopts a significantly lower absolute value with $\alpha = -7.3$, which now also agrees well with the values in the literature [39,16]. Whereas a low absolute value for α cannot represent the distinct nonlinearity of the stress–strain curve already for strains $< 10\%$, a high absolute value predicts unrealistically high stresses for large strains or multiaxial loading cases. For the sequence of multiple uniaxial loading modes, we limited ourselves to 10% strain in compression and tension, and 20% in shear, to not damage the tissue during the course

of the experiment. As the stress–strain curve exhibits a distinct nonlinearity even for those relatively small strains, the value α obtained from protocol 1 would predict unrealistically high stresses for larger strains. This demonstrates that the one-term Ogden model can easily predict an unrealistic behavior when exceeding the deformation range used for parameter identification. Consequently, whereas the sequence of loading modes performed in protocol 1 allows for an accurate calibration of the parameter μ , it is not suitable to calibrate α .

We conclude that the one-term Ogden model is able to capture the mechanical response of human brain tissue under multiaxial loading modes. However, particularly caution is necessary when determining the parameter α : the compression–tension asymmetry pre-supposes a negative sign for α and high absolute values yield unrealistically high stresses for large strains and multiaxial loading cases.

5. Limitations

A major limitation of this study is that we tested human brain tissue *in vitro*. Undoubtedly, the deformations imposed by uniaxial compression and extension, simple shear and combined compression/tension–shear testing differ from those experienced *in vivo*. Furthermore, due to the ultrasoft nature of brain tissue, it deforms during specimen preparation and handling. This implies a variation of specimen size and shape, which, upon mounting the samples, were no longer perfectly cuboidal with 5 mm side length. The slightly varying specimen heights resulted in small differences in strain rates, which also applied to the different stretch levels during protocol 2. However, preliminary experiments had shown that in the slow-loading-rate regime conducted in the current study, the sensitivity towards strain rate was insignificant. Furthermore, nonuniform specimen dimensions or potential changes in the tissue state after death inevitably blur the true extent of regional and directional differences. For example, asymmetric mounting or specimen dimensions could misleadingly imply an anisotropic mechanical response or a potential contribution of nerve fibers could be lost when those are dead. Similarly, irregularities in the tissue's microstructure can alter the results. To minimize the limitation of nonuniform orientation of nerve fibers across each specimen we only used samples from the corpus callosum to study directional dependencies.

Besides, post-mortem time could potentially affect brain tissue properties. The time lapses between death and autopsy, duration times for MRI investigations, preparation, and testing resulted in a maximum time period of 60 h after death. While studies on porcine brain tissue revealed a slight increase in tissue stiffness beginning 6 h post-mortem [31,32], other experiments on bovine brain tissue showed no change in tissue stiffness between two hours and five days post mortem [30,28]. In the current time window, we could not observe a notable change in tissue stiffness between samples that were tested first and last.

We conducted all tests at room temperature. Although we expect a slight influence of temperature on the mechanical properties of the tissue, the main purpose of this study was to understand directional and regional dependencies under multiple loading modes. Thus, the disadvantages mentioned in Section 2.4 were deemed too costly relative to the potential benefits. Within the past decade, magnetic resonance elastography has rapidly advanced as a non-invasive *in vivo* tool, to measure elastic properties of living human brain tissue. However, results have varied tremendously, both qualitatively and quantitatively [23,24,27,64], as they highly depend on the method used to extract elastic properties or excitation frequencies. Despite the fact that this technology is still in its infancy [21], it remains questionable whether it is

suitable to quantify regional and directional mechanical properties of human brain tissue [65]. Thus, although the issues associated with *in vitro* mechanical testing may limit the reliability of explicit material parameter identification, the approach used here has provided important novel insights into regional and directional properties of human brain tissue under multiple loading modes. We distinguished between structurally different regions, the corpus callosum, the corona radiata, the basal ganglia, and the cortex. However, our experiments show that this classification does not necessarily hold for the elastic response of the tissue. In the future regional studies could therefore differentiate between regions of similar microstructure.

In terms of constitutive modeling, we focused on the hyperelastic, pre-conditioned behavior of human brain tissue. This assumption holds for sufficiently slow deformations, for example, during brain development [70]. On shorter time scales, brain tissue is a highly viscous and porous material [18,36,37]. To additionally account for conditioning effects during the first loading cycle and the highly hysteretic behavior, we will extend the time-independent hyperelastic formulation presented in the current study to time-dependent contributions [46]. Here, the question arises whether brain tissue should be modeled as a single phase viscous solid [57] or as a dual phase fluid-saturated solid [37,71,72], which to answer would require additional experiments and goes beyond the scope of the present work. We further note that experiments towards the understanding of the porous nature of the tissue can barely be performed for multiple loading modes on one sample. Thus, only a combination with the loading-mode specific considerations presented here will enable us to eventually capture the behavior of human brain tissue for all time scales and arbitrary loading conditions. In addition, further experiments should be conducted to better understand the rate-dependency of regional differences indicated in Section 4.4.

6. Conclusion

In the present paper we documented experimental data obtained from a sequence of three individual loading modes (simple shear in two orthogonal directions, unconfined compression, extension) on human brain specimens in addition to mixed modes combining compression/tension with shear. For the first time we tested the *same* specimen with these different loading modes. The biomechanical tests were performed on the corpus callosum, the corona radiata, the basal ganglia and the cortex in combination with antecedent DTI to identify to which extent the axonal networks contribute to the macroscopic constitutive response. We characterized the loading-mode specific regional and directional behavior of the human brain tissue and discussed pre-conditioning and hysteresis effects. The results demonstrated that the human brain tissue is highly nonlinear and viscoelastic, with a pronounced compression–tension asymmetry. The elastic response of the human brain tissue under all loading modes (here elastic is defined as the average between loading and unloading) is best described by a modified one-term Ogden model, which also captures the compression–tension asymmetry.

Although we used a constitutive model to capture the elastic component of brain tissue deformation, in a subsequent step a viscoelastic model is required to also capture the involved dissipative mechanism. However, the knowledge of the elastic properties of human brain tissues under various loading modes and the related constitutive model is valuable to better determine injury criteria, to help improve neurosurgical procedures, and to develop better smart protection systems. Since the provided elastic constitutive model is based on the described systematic tissue characterization it is valuable for complex computational simulations with varying

loading conditions. More advanced fast imaging techniques and new MR sequences will allow increased temporal and spatial resolution in future studies.

Acknowledgements

This study was supported by the German National Science Foundation grant STE 544/50 to SB and PS, by the National Institutes of Health grant U54GM072970, and by the Humboldt Research Award to EK. The Austrian Science Fund supported CB and CL (FWF project KLI-523).

References

- [1] A. Goriely, M.G. Geers, G.A. Holzapfel, J. Jayamohan, A. Jérusalem, S. Sivaloganathan, W. Squier, J.A. van Dommelen, S. Waters, E. Kuhl, Mechanics of the brain: perspectives, challenges, and opportunities, *Biomech. Model. Mechanobiol.* 14 (2015) 931–965.
- [2] R.J.H. Cloots, J.A.W. Van Dommelen, S. Kleiven, M.G.D. Geers, Multi-scale mechanics of traumatic brain injury: predicting axonal strains from head loads, *Biomech. Model. Mechanobiol.* 12 (2013) 137–150.
- [3] B. Harding, R.A. Risdon, H.F. Krous, Shaken baby syndrome, *BMJ* 328 (2004) 720–721.
- [4] A. Kansal, S. Torquato, G. Harsh, E. Chiocia, T. Deisboeck, Simulated brain tumor growth dynamics using a three-dimensional cellular automaton, *J. Theor. Biol.* 203 (2000) 367–382.
- [5] D.P. Richman, R.M. Stewart, J. Hutchinson, V.S. Cavincss Jr, Mechanical mode of brain convolutional development, *Science* 189 (1975) 18–21.
- [6] S. Budday, P. Steinmann, E. Kuhl, The role of mechanics during brain development, *J. Mech. Phys. Solids* 72 (2014) 75–92.
- [7] T. Tallinen, J.Y. Chung, F. Rousseau, N. Girard, J. Lefèvre, L. Mahadevan, On the growth and form of cortical convolutions, *Nat. Phys.* 12 (2016) 588–593.
- [8] R.J.H. Cloots, J.A.W. Van Dommelen, M.G.D. Geers, A tissue-level anisotropic criterion for brain injury based on microstructural axonal deformation, *J. Mech. Behav. Biomed. Mater.* 5 (2012) 41–52.
- [9] L.C. Wu, V. Nangia, K. Bui, B. Hammor, M. Kurt, F. Hernandez, C. Kuo, D.B. Camarillo, In vivo evaluation of wearable head impact sensors, *Ann. Biomed. Eng.* 44 (2016) 1234–1245.
- [10] K.P. Wilkie, C.S. Drapaca, S. Sivaloganathan, Aging impact on brain biomechanics with applications to hydrocephalus, *Math. Med. Biol.* 29 (2012) 145–161.
- [11] A. Goriely, S. Budday, E. Kuhl, Neuromechanics: from neurons to brain, *Adv. Appl. Mech.* 48 (2015) 79–139.
- [12] K. Miller, *Biomechanics of the Brain*, Springer Science & Business Media, 2011.
- [13] K.L. Thibault, S.S. Margulies, Age-dependent material properties of the porcine cerebrum: effect on pediatric inertial head injury criteria, *J. Biomech.* 31 (1998) 1119–1126.
- [14] L.Z. Shuck, S.H. Advani, Rheological response of human brain tissue in shear, *J. Basic Eng.* 94 (1972) 905–911.
- [15] M.T. Prange, S.S. Margulies, Regional, directional, and age-dependent properties of the brain undergoing large deformation, *J. Biomech. Eng.* 124 (2002) 244–252.
- [16] F. Velardi, F. Fraternali, M. Angelillo, Anisotropic constitutive equations and experimental tensile behavior of brain tissue, *Biomech. Model. Mechanobiol.* 5 (2006) 53–61.
- [17] Y. Feng, R.J. Okamoto, R. Namani, G.M. Genin, P.V. Bayly, Measurements of mechanical anisotropy in brain tissue and implications for transversely isotropic material models of white matter, *J. Mech. Behav. Biomed. Mater.* 23 (2013) 117–132.
- [18] X. Jin, F. Zhu, H. Mao, M. Shen, K.H. Yang, A comprehensive experimental study on material properties of human brain tissue, *J. Biomech.* 46 (2013) 2795–2801.
- [19] A. Gefen, N. Gefen, Q. Zhu, R. Raghupathi, S.S. Margulies, Age-dependent changes in material properties of the brain and braincase of the rat, *J. Neurotrauma* 20 (2003) 1163–1177.
- [20] B.S. Elkin, A. Ilankovan, B. Morrison, Age-dependent regional mechanical properties of the rat hippocampus and cortex, *J. Biomech. Eng.* 132 (2010) 011010.
- [21] S. Chatelin, J. Vappou, S. Roth, J.-S. Raul, R. Willinger, Towards child versus adult brain mechanical properties, *J. Mech. Behav. Biomed. Mater.* 6 (2012) 166–173.
- [22] J.D. Finan, B.S. Elkin, E.M. Pearson, I.L. Kalbian, B. Morrison III, Viscoelastic properties of the rat brain in the sagittal plane: effects of anatomical structure and age, *Ann. Biomed. Eng.* 40 (2012) 70–78.
- [23] P.J. McCracken, A. Manduca, J. Felmlee, R.L. Ehman, Mechanical transient-based magnetic resonance elastography, *Magn. Reson. Med.* 53 (2005) 628–639.
- [24] M.A. Green, L.E. Bilston, R. Sinkus, In vivo brain viscoelastic properties measured by magnetic resonance elastography, *NMR Biomed.* 21 (2008) 755–764.
- [25] A.F. Christ, K. Franze, H. Gautier, P. Moshayedi, J. Fawcett, R.J. Franklin, R.T. Karadottir, J. Guck, Mechanical difference between white and gray matter in the rat cerebellum measured by scanning force microscopy, *J. Biomech.* 43 (2010) 2986–2992.
- [26] J.A.W. Van Dommelen, T.P.J. Van der Sande, M. Hrapko, G.W.M. Peters, Mechanical properties of brain tissue by indentation: interregional variation, *J. Mech. Behav. Biomed. Mater.* 3 (2010) 158–166.
- [27] C.L. Johnson, M.D. McGarry, A.A. Gharibans, J.B. Weaver, K.D. Paulsen, H. Wang, W.C. Olivero, B.P. Sutton, J.G. Georgiadis, Local mechanical properties of white matter structures in the human brain, *Neuroimage* 79 (2013) 145–152.
- [28] S. Budday, R. Nay, R. de Rooij, P. Steinmann, T. Wyrobek, T.C. Ovaert, E. Kuhl, Mechanical properties of gray and white matter brain tissue by indentation, *J. Mech. Behav. Biomed. Mater.* 46 (2015) 318–330.
- [29] J. Weickenmeier, R. de Rooij, S. Budday, P. Steinmann, T.C. Ovaert, E. Kuhl, Brain stiffness increases with myelin content, *Acta Biomater.* 42 (2016) 265–272.
- [30] K. Darvish, J.R. Crandall, Nonlinear viscoelastic effects in oscillatory shear deformation of brain tissue, *Med. Eng. Phys.* 9 (2001) 633–645.
- [31] S. Nicolle, M. Lounis, R. Willinger, Shear properties of brain tissue over a frequency range relevant for automotive impact situations: new experimental results, *Stapp Car Crash J.* 48 (2004) 239–258.
- [32] A. Garo, M. Hrapko, J.A.W. Van Dommelen, G.W.M. Peters, Towards a reliable characterisation of the mechanical behaviour of brain tissue: the effects of post-mortem time and sample preparation, *Biorheology* 44 (2007) 51–58.
- [33] G. Fallenstein, V.D. Hulce, J.W. Melvin, Dynamic mechanical properties of human brain tissue, *J. Biomech.* 2 (1969) 217–226.
- [34] M.S. Estes, J.H. McElhaney, Response of brain tissue to compressive loading, 1970. ASME Paper, No. 70-BHF-13.
- [35] J.E. Galford, J.H. McElhaney, A viscoelastic study of scalp, brain, and dura, *J. Biomech.* 3 (1970) 211–221.
- [36] B.R. Donnelly, J. Medige, Shear properties of human brain tissue, *J. Biomech. Eng.* 119 (1997) 423–432.
- [37] G. Franceschini, D. Bigoni, P. Regitnig, G.A. Holzapfel, Brain tissue deforms similarly to filled elastomers and follows consolidation theory, *J. Mech. Phys. Solids* 54 (2006) 2592–2620.
- [38] K. Miller, K. Chinzei, Constitutive modelling of brain tissue: experiment and theory, *J. Biomech.* 30 (1997) 1115–1121.
- [39] K. Miller, K. Chinzei, Mechanical properties of brain tissue in tension, *J. Biomech.* 35 (2002) 483–490.
- [40] B. Rashid, M. Destrade, M.D. Gilchrist, Mechanical characterization of brain tissue in compression at dynamic strain rates, *J. Mech. Behav. Biomed. Mater.* 10 (2012) 23–38.
- [41] B. Rashid, M. Destrade, M.D. Gilchrist, Mechanical characterization of brain tissue in simple shear at dynamic strain rates, *J. Mech. Behav. Biomed. Mater.* 28 (2013) 71–85.
- [42] B. Rashid, M. Destrade, M.D. Gilchrist, Mechanical characterization of brain tissue in tension at dynamic strain rates, *J. Mech. Behav. Biomed. Mater.* 33 (2014) 43–54.
- [43] L.E. Bilston, Z. Liu, N. Phan-Thien, Large strain behaviour of brain tissue in shear: some experimental data and differential constitutive model, *Biorheology* 38 (2001) 335–345.
- [44] K. Pogoda, L. Chin, P.C. Georges, F.J. Byfield, R. Bucki, R. Kim, M. Weaver, R.G. Wells, C. Marcinkiewicz, P.A. Janney, Compression stiffening of brain and its effect on mechanosensing by glioma cells, *New J. Phys.* 16 (2014) 075002.
- [45] G. Sommer, A.J. Schriefel, M. Andrä, M. Sacherer, C. Viertler, H. Wolinski, G.A. Holzapfel, Biomechanical properties and microstructure of human ventricular myocardium, *Acta Biomater.* 24 (2015) 172–192.
- [46] R. de Rooij, E. Kuhl, Constitutive modeling of brain tissue: current perspectives, *Appl. Mech. Rev.* 68 (2016) 010801.
- [47] T. Kaster, I. Sack, A. Samani, Measurement of the hyperelastic properties of ex vivo brain tissue slices, *J. Biomech.* 44 (2011) 1158–1163.
- [48] R. Moran, J.H. Smith, J.J. Garça, Fitted hyperelastic parameters for human brain tissue from reported tension, compression, and shear tests, *J. Biomech.* 47 (2014) 3762–3766.
- [49] R.W. Ogden, Large deformation isotropic elasticity—on the correlation of theory and experiment for incompressible rubberlike solids, *Proceedings of the Royal Society of London A: Mathematical, Physical and Engineering Sciences*, vol. 326, The Royal Society, 1972, pp. 565–584.
- [50] H. Demiray, A note on the elasticity of soft biological tissues, *J. Biomech.* 5 (1972) 309–311.
- [51] A. Gent, A new constitutive relation for rubber, *Rubber Chem. Technol.* 69 (1996) 59–61.
- [52] G.A. Holzapfel, *Nonlinear Solid Mechanics. A Continuum Approach for Engineering*, John Wiley & Sons, Chichester, 2000.
- [53] L.A. Mihai, L. Chin, P.A. Janney, A. Goriely, A comparison of hyperelastic constitutive models applicable to brain and fat tissues, *J. R. Soc. Interface* 12 (2015) 20150486.
- [54] S. Smith, M. Jenkinson, M. Woolrich, C. Beckmann, T. Behrens, H. Johansen-Berg, P. Bannister, M. De Luca, I. Drobniak, D. Flitney, R. Niazy, J. Saunders, J. Vickers, Y. Zhang, N. De Stefano, J. Brady, P. Matthews, Advances in functional and structural MR image analysis and implementation as FSL, *Neuroimage* 23 (2004) 208–219.
- [55] M. Woolrich, S. Jbabdi, B. Patenaude, M. Chappell, S. Makni, T. Behrens, C. Beckmann, M. Jenkinson, S. Smith, Bayesian analysis of neuroimaging data in FSL, *Neuroimage* 45 (2009) 173–186.
- [56] G. Sommer, M. Eder, L. Kovacs, H. Pathak, L. Bonitz, C. Mueller, P. Regitnig, G.A. Holzapfel, Multiaxial mechanical properties and constitutive modeling of

- human adipose tissue: a basis for preoperative simulations in plastic and reconstructive surgery, *Acta Biomater.* 9 (2013) 9036–9048.
- [57] T.P. Prevost, A. Balakrishnan, S. Suresh, S. Socrate, Biomechanics of brain tissue, *Acta Biomater.* 7 (2011) 83–95.
- [58] A. Jérusalem, M. Dao, Continuum modeling of a neuronal cell under blast loading, *Acta Biomater.* 8 (2012) 3360–3371.
- [59] G.A. Holzapfel, R.W. Ogden, Constitutive modelling of arteries, *Proc. R. Soc. London A* 466 (2010) 1551–1597.
- [60] F. Pervin, W.W. Chen, Dynamic mechanical response of bovine gray matter and white matter brain tissues under compression, *J. Biomech.* 42 (2009) 731–735.
- [61] R. Lindenberg, R.S. Fisher, S.H. Durlacher, W.V. Lovitt Jr, E. Freytag, Lesions of the corpus callosum following blunt mechanical trauma to the head, *Am. J. Pathol.* 31 (1955) 297–317.
- [62] K.M. Cecil, E.C. Hills, M.E. Sandel, D.H. Smith, T.K. McIntosh, L.J. Mannon, G.P. Sinson, L.J. Bagley, R.I. Grossman, R.E. Lenkinski, Proton magnetic resonance spectroscopy for detection of axonal injury in the splenium of the corpus callosum of brain-injured patients, *J. Neurosurg.* 88 (1998) 795–801.
- [63] D.E. Koser, E. Moeendarbary, J. Hanne, S. Kuerten, K. Franze, CNS cell distribution and axon orientation determine local spinal cord mechanical properties, *Biophys. J.* 108 (2015) 2137–2147.
- [64] S.A. Kruse, G.H. Rose, K.J. Glaser, A. Manduca, J.P. Felmlee, C.R. Jack, R.L. Ehman, Magnetic resonance elastography of the brain, *Neuroimage* 39 (2008) 231–237.
- [65] S. Papazoglou, S. Hirsch, J. Braun, I. Sack, Multifrequency inversion in magnetic resonance elastography, *Phys. Med. Biol.* 57 (2012) 2329.
- [66] K.P. Whittall, A.L. Mackay, D.A. Graeb, R.A. Nugent, D.K. Li, D.W. Paty, In vivo measurement of T2 distributions and water contents in normal human brain, *Magn. Reson. Med.* 37 (1997) 34–43.
- [67] A. Baborie, W. Kuschinsky, Lack of relationship between cellular density and either capillary density or metabolic rate in different regions of the brain, *Neurosci. Lett.* 404 (2006) 20–22.
- [68] M. Cavaglia, S.M. Dombrowski, J. Drazba, A. Vasanji, P.M. Bokesch, D. Janigro, Regional variation in brain capillary density and vascular response to ischemia, *Brain Res.* 910 (2001) 81–93.
- [69] C.T. McKee, J.A. Last, P. Russell, C.J. Murphy, Indentation versus tensile measurements of Young's modulus for soft biological tissues, *Tissue Eng. Part B: Rev.* 17 (2011) 155–164.
- [70] S. Budday, C. Raybaud, E. Kuhl, A mechanical model predicts morphological abnormalities in the developing human brain, *Sci. Rep.* 4 (2014) 5644.
- [71] S. Cheng, L.E. Bilston, Unconfined compression of white matter, *J. Biomech.* 40 (2007) 117–124.
- [72] W. Ehlers, A. Wagner, Multi-component modelling of human brain tissue: a contribution to the constitutive and computational description of deformation, flow and diffusion processes with application to the invasive drug-delivery problem, *Comput. Methods Biomech. Biomed. Eng.* 18 (2015) 861–879.